



**HAL**  
open science

## Irreversible deformation of hyper-crosslinked polymers after hydrogen adsorption

Pamela Ramirez-Vidal, Fabián Suárez-García, Rafael L.S. Canevesi, Alberto Castro-Muñiz, Philippe Gadonneix, Juan Ignacio Paredes, Rafael L S Canevesi, Alain Celzard, Vanessa Fierro

► **To cite this version:**

Pamela Ramirez-Vidal, Fabián Suárez-García, Rafael L.S. Canevesi, Alberto Castro-Muñiz, Philippe Gadonneix, et al.. Irreversible deformation of hyper-crosslinked polymers after hydrogen adsorption. *Journal of Colloid and Interface Science*, 2022, 605, pp.513-527. 10.1016/j.jcis.2021.07.104 . hal-03317143

**HAL Id: hal-03317143**

**<https://hal.univ-lorraine.fr/hal-03317143v1>**

Submitted on 6 Aug 2021

**HAL** is a multi-disciplinary open access archive for the deposit and dissemination of scientific research documents, whether they are published or not. The documents may come from teaching and research institutions in France or abroad, or from public or private research centers.

L'archive ouverte pluridisciplinaire **HAL**, est destinée au dépôt et à la diffusion de documents scientifiques de niveau recherche, publiés ou non, émanant des établissements d'enseignement et de recherche français ou étrangers, des laboratoires publics ou privés.

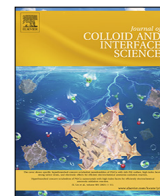


Distributed under a Creative Commons Attribution - NonCommercial - NoDerivatives 4.0 International License



Contents lists available at ScienceDirect

Journal of Colloid and Interface Science

journal homepage: [www.elsevier.com/locate/jcis](http://www.elsevier.com/locate/jcis)

# Irreversible deformation of hyper-crosslinked polymers after hydrogen adsorption

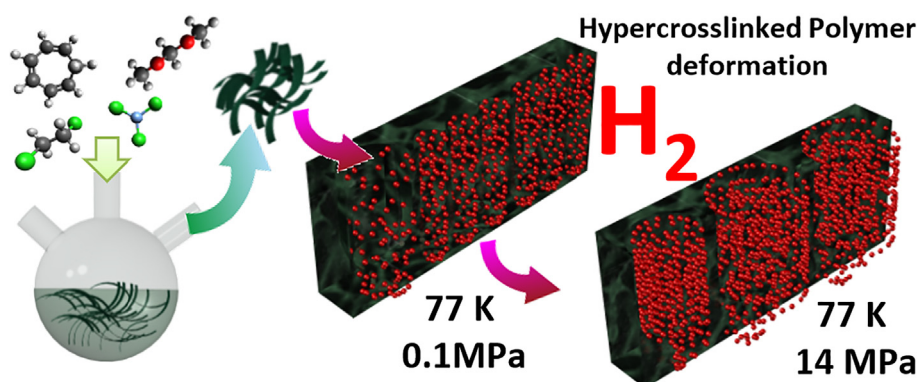


Pamela Ramirez-Vidal<sup>a</sup>, Fabián Suárez-García<sup>b,\*</sup>, Rafael L.S. Canevesi<sup>a</sup>, Alberto Castro-Muñiz<sup>b</sup>, Philippe Gadonneix<sup>a</sup>, Juan Ignacio Paredes<sup>b</sup>, Alain Celzard<sup>a</sup>, Vanessa Fierro<sup>a,\*</sup>

<sup>a</sup>Institut Jean Lamour (IJL), Université de Lorraine, CNRS, F-88000 Epinal, France

<sup>b</sup>Instituto de Ciencia y Tecnología del Carbono, INCAR-CSIC, c/Francisco Pintado Fe, 26, 33011 Oviedo, Spain

## GRAPHICAL ABSTRACT



## ARTICLE INFO

### Article history:

Received 30 May 2021

Revised 16 July 2021

Accepted 19 July 2021

Available online 24 July 2021

### Keywords:

Hyper-crosslinked polymers

Graphene oxide

Microporous organic materials

Friedel-Crafts reaction

High-pressure H<sub>2</sub> adsorption

## ABSTRACT

Hyper-crosslinked polymers (HCPs) have been produced by the Friedel-Crafts reaction using anthracene, benzene, carbazole or dibenzothiophene as precursors and dimethoxymethane as crosslinker, and the effect of graphene oxide (GO) addition has been studied. The resulting HCPs were highly microporous with BET areas ( $A_{\text{BET}}$ ) between 590 and 1120 m<sup>2</sup> g<sup>-1</sup>. The benzene-derived HCP (B1FeM2) and the corresponding composite with GO (B1FeM2-GO) exhibited the highest  $A_{\text{BET}}$  and were selected to study their hydrogen adsorption capacities in the pressure range of 0.1 – 14 MPa at 77 K. The maximum H<sub>2</sub> excess uptake was 2.1 and 2.0 wt% for B1FeM2 and B1FeM2-GO, respectively, at 4 MPa and 77 K. The addition of GO reduced the specific surface area but increased the density of the resultant HCP-GO composites, which is beneficial for practical applications and proves that materials giving higher gravimetric storage capacities are not necessarily those that offer higher volumetric capacities. H<sub>2</sub> adsorption-desorption cycles up to 14 MPa showed irreversible deformation of both HCP and HCP-GO materials, which calls into question their application for hydrogen adsorption at pressures above 4 MPa.

© 2021 The Authors. Published by Elsevier Inc. This is an open access article under the CC BY-NC-ND license (<http://creativecommons.org/licenses/by-nc-nd/4.0/>).

## 1. Introduction

With the highest gravimetric energy density of all non-nuclear fuels (39.4 kWh kg<sup>-1</sup>) hydrogen is a promising energy vector that could reduce the dependence on fossil fuels, whose energy density

\* Corresponding authors.

E-mail addresses: [Fabian.suarez@csic.es](mailto:Fabian.suarez@csic.es) (F. Suárez-García), [Vanessa.Fierro@univ-lorraine.fr](mailto:Vanessa.Fierro@univ-lorraine.fr) (V. Fierro).

<https://doi.org/10.1016/j.jcis.2021.07.104>

0021-9797/© 2021 The Authors. Published by Elsevier Inc.

This is an open access article under the CC BY-NC-ND license (<http://creativecommons.org/licenses/by-nc-nd/4.0/>).

is 13.1 kWh kg<sup>-1</sup> for liquid hydrocarbons [1]. However, hydrogen is also the lightest element, which makes it challenging to store safely, compactly and inexpensively. One of the main problems is the volume of the tank needed for practical applications. Indeed, 5 kg of hydrogen, equivalent to 61 m<sup>3</sup> at 298 K and 0.1 MPa, would be needed in a combustion engine to travel 500 km [2]. In order to increase the volumetric energy density, hydrogen has been stored as: (i) liquid hydrogen in cryogenic tanks [3,4]; (ii) compressed hydrogen in gas cylinders at very high pressure [5,6]; and (iii) adsorbed and absorbed hydrogen in solids: metal hydrides [7,8], metallic-organic frameworks [9–11], nanostructured carbons [12–14], and hyper-crosslinked polymers (HCPs) [15,16], among others. Due to its low cost and feasibility, physical sorption of H<sub>2</sub> in porous materials is one of the most studied approaches for hydrogen storage. H<sub>2</sub> adsorption is a process that occurs at low temperatures through van der Waals interactions with a solid [1]. It is well known that, in order to increase H<sub>2</sub> storage capacity by adsorption in a material, the presence of a developed microporous surface is necessary as the phenomenon is enhanced in very narrow pores by the overlapping adsorption potentials [14].

HCPs are particularly attractive for H<sub>2</sub> storage due to their high surface area, as well as thermal and chemical stability. The synthesis of HCPs is potentially suitable for large-scale production because it uses mild synthesis conditions as well as simple and inexpensive monomers and solvents [17–19]. Friedel-Crafts alkylation is one of the most widely used methods for the synthesis of HCPs [20–22]. It has the advantage of forming polymer networks with crosslinking degrees above 40%. The latter leads to rigid networks with permanent micropores, high micropore volume and high specific surface area [17,23]. HCPs have been applied to gas storage and separation [24–29]. H<sub>2</sub> adsorption capacities at 77 K and 0.1 MPa range from 0.5 to 1.9 wt% for HCPs with surface areas between 500 and 1845 m<sup>2</sup> g<sup>-1</sup> [18,20–22,24,30–39]. In addition, hydrogen uptake in HCPs can be increased when the adsorbents are submitted to high pressures of H<sub>2</sub> [20,31,40–43]. For instance, hydrogen uptake increased from 1.61 to 3.68 wt% when increasing pressure from 0.1 to 1.5 MPa at 77 K using an HCP with a specific surface area of 1904 m<sup>2</sup> g<sup>-1</sup> [42].

Furthermore, some studies have proposed to improve the adsorption properties of HCPs by adding different functional nanostructured materials to improve their gas sorption selectivity, gas storage capacity or ability to capture organic pollutants [23,44–46]. Nanostructured carbon materials such as multi-walled carbon nanotubes (MWCNTs), graphene oxide (GO) and graphene nanoplatelets (GNPs) [23,45,46] have been tested as potential candidates to improve HCP materials. Especially, GO-based nanocomposites have shown remarkable mechanical, electrical, thermal, and barrier properties over the last decade [47].

Herein, three series of HCP materials were produced by the “knitting” strategy as reported by Li et al. [18]. The first series was prepared using different molar ratios of carbazole (or the HCP precursor monomer) to catalyst (FeCl<sub>3</sub>). A second series of materials was synthesised using four different HCP precursor monomers (anthracene, benzene, carbazole or dibenzothiophene) in order to study the influence of the chemical nature of the monomer in the synthesis. The third series was prepared by adding GO to the reaction medium. Finally, benzene-based HCPs and their HCP-GO composites were selected to study their hydrogen adsorption performance at 77 K, over a pressure range of 0.1 to 14 MPa.

## 2. Experimental

### 2.1. Synthesis of hyper-crosslinked polymers (HCPs)

Reagents from Sigma-Aldrich were used as HCP precursors: anthracene (97% pure), benzene (99.8%), carbazole (99.8%) or dibenzothiophene (98%). The procedure that was followed has been reported elsewhere [18] and is illustrated in Fig. 1. In short, the monomer selected from the four studied here was added to 100 mL of 1,2-dichloroethane and the mixture was heated up to 338 K under an inert atmosphere (nitrogen). The crosslinker, dimethoxymethane (99%, Sigma-Aldrich) and the catalyst, FeCl<sub>3</sub> (98%, Sigma-Aldrich) were poured into the dispersion when the temperature reached 338 K and 353 K, respectively. The reaction was maintained at 353 K under reflux in an inert atmosphere for 24 h. The reaction product was first filtered, washed with methanol and subsequently dispersed in 200 mL of 1 M HCl for 1 h to eliminate the catalyst. Then, the solid was filtered again and washed extensively with methanol using a Soxhlet extractor for 24 h. The recovered paste-like material was dried under vacuum at 353 K for 12 h.

In order to study the effect of the precursor, the addition of GO and the amount of catalyst on the properties of the resulting polymers, three series of materials were synthesised:

- The first series of materials was synthesised using carbazole as a precursor in the presence of different amounts of catalyst. The amounts used in each reaction were 50, 10 and 10 mmol for the carbazole with 100, 10 and 2 mmol of FeCl<sub>3</sub>, respectively. The molar amount of crosslinker, dimethoxymethane, was twice that of the precursor for all syntheses. Thus, the monomer/catalyst/crosslinker molar ratios studied here were 1:2:2; 1:1:2 and 1:0.2:2, respectively).
- The second series of materials was prepared using different monomers: anthracene (A), benzene (B), carbazole (C) or dibenzothiophene (D) as precursors using monomer/FeCl<sub>3</sub>/dimethoxymethane molar ratios of 1:1:2 (i.e., 10/10/20 mmol).
- The third series was prepared by adding GO to the synthesis medium. First, graphite oxide was produced from natural graphite powder (Sigma-Aldrich) by the Hummers method [48,49]. After purification with a 1% HCl solution and large volumes of deionised water, the oxidised product was filtered and dried at 333 K for 12 h under vacuum. Then, 50 mg of GO was dispersed in 100 mL of 1,2-dichloroethane and sonicated for 30 min under an inert atmosphere (nitrogen). The rest of the synthesis conditions were kept unchanged. In this series, monomer/FeCl<sub>3</sub>/dimethoxymethane of molar ratios of 1:1:2 were used.

The synthesised samples were labelled ZxFyM2x, where Z corresponds to monomer A, B, C or D for anthracene, benzene, carbazole or dibenzothiophene, respectively, and x, y and 2x correspond to the molar ratios of monomer, FeCl<sub>3</sub> (referred to as Fe) and dimethoxymethane (referred to as M), respectively, used in the synthesis.

### 2.2. Characterisation of HCPs and HCP-GO composites

Thermogravimetric (TG) analysis of the samples was performed in a CI Electronics microbalance under argon and air atmosphere

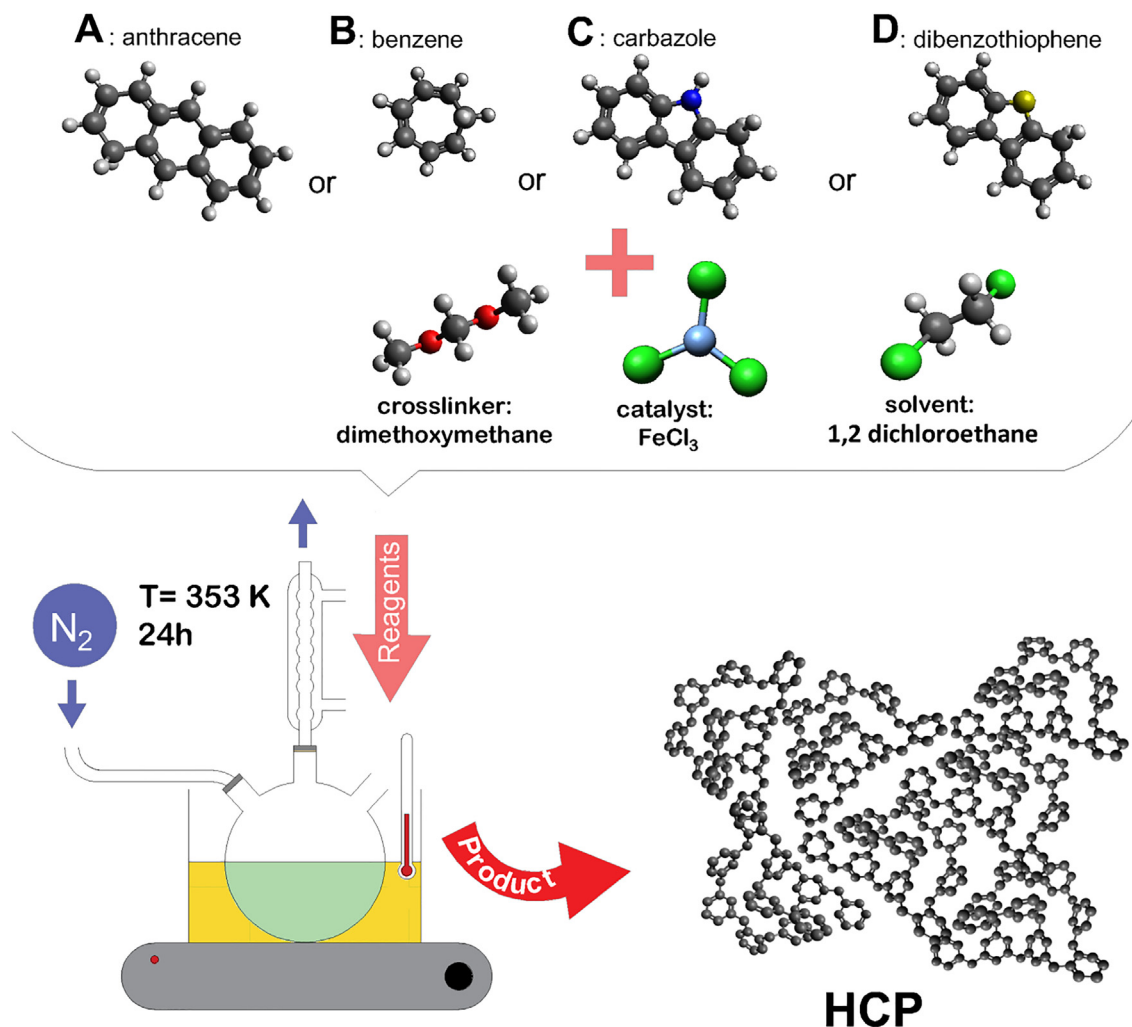


**Fig. 1.** Schematic diagram of the synthetic route to hyper-crosslinked polymers (HCPs). The monomers used were anthracene (A), benzene (B), carbazole (C) and dibenzothiophene (D).

(flow rate  $50 \text{ mL min}^{-1}$ ) by increasing the temperature at a rate of  $10 \text{ K min}^{-1}$  up to  $1223 \text{ K}$ , where a dwell time of  $1 \text{ h}$  was set. Elemental analysis (EA) of the HCPs and composites was carried out in an Elementar Vario EL Cube analyser to determine the contents of oxygen, hydrogen, carbon, nitrogen and sulphur.

In order to study the microstructural changes of the samples upon addition of GO, selected samples were characterised by scanning electron microscopy (SEM) in a Zeiss Auriga 40 FIB-SEM with secondary electron detector at low accelerating voltage ( $1 \text{ kV}$ ).

The skeletal density of the samples was determined by He pycnometry in a Micromeritics® AccuPyc II 1340 apparatus at room temperature. Prior to measurement, the samples were outgassed at  $353 \text{ K}$  under primary vacuum overnight. The tapped density of the samples was determined in a Quantachrome® Autotap instrument. For this purpose, after outgassing the samples at  $353 \text{ K}$  under primary vacuum overnight, a volume of approximately  $4 \text{ mL}$  of solid was poured into a  $10 \text{ mL}$  measuring cylinder and mechanically tapped 5000 times. The determination was repeated twice and if a variation of  $>5\%$  was observed, a third determination was performed. The tapped density was calculated as the mass of the sample divided by the bed volume averaged over two (or three) tapping experiment determinations.

Textural characterisation of the HCPs and their composites was performed by  $\text{N}_2$ ,  $\text{CO}_2$  and  $\text{H}_2$  physisorption, at  $77$ ,  $273$  and  $77 \text{ K}$ , respectively, in a Micromeritics® 3-flex manometric apparatus.

Prior to the gas adsorption experiments, the samples were outgassed under secondary vacuum ( $<10^{-4} \text{ Pa}$ ) at  $333 \text{ K}$  for  $>24 \text{ h}$ . This temperature was chosen to ensure that the sample would not degrade during outgassing. Although the samples are stable up to  $523 \text{ K}$  under atmospheric pressure ( $10^5 \text{ Pa}$ ), according to our experience, degradation could start at  $353 \text{ K}$  under secondary vacuum ( $<10^{-4} \text{ Pa}$ ). The BET area ( $A_{\text{BET}}$ ) was calculated from the  $\text{N}_2$  isotherms using the Micromeritics® Microactive software and taking into account the Rouquerol criterion [50]. The 2D non-local density functional theory for heterogeneous surfaces (2D-NLDFT-HS) was applied to both  $\text{N}_2 + \text{CO}_2$  and  $\text{N}_2 + \text{H}_2$  isotherms using the SAIEUS® software (Micromeritics) to obtain the pore size distributions (PSDs) of HCPs and their composites [51–53]. From their PSDs, we obtained the specific surface area ( $S_{\text{NLDFT}}$ ), and the volumes of ultramicropores ( $V_{<0.7, \text{NLDFT}}$ ), supermicropores ( $V_{0.7-2, \text{NLDFT}}$ ), mesopores ( $V_{\text{mes}}$ ), as well as the total pore volume ( $V_{\text{T}}$ ). It is worth mentioning that we used the kernels developed for carbon materials, as there are no kernels explicitly dedicated to HCPs.

### 2.3. Hydrogen adsorption at high pressure

The two materials with the highest specific surface areas, an HCP and an HCP-GO composite, were selected for high-pressure hydrogen adsorption testing at  $77 \text{ K}$  and up to  $14 \text{ MPa}$ , using a Micromeritics® HPVAIL instrument coupled to a single-stage closed

cycle cryogenic refrigerator using a He compressor to produce the cold temperatures. About 0.8 g of sample was outgassed under vacuum ( $6 \times 10^{-4}$  Pa) at 333 K overnight, prior to measurement. After the first H<sub>2</sub> adsorption (up to 14 MPa) – desorption isotherms, four more consecutive adsorption–desorption isotherms were carried out on the same samples. After the first cycle, the samples were outgassed in the measuring port at room temperature under vacuum ( $6 \times 10^{-4}$  Pa) for 12, 33, 50 and 72 h, for the second, third, fourth and fifth isotherms, respectively.

### 3. Results and discussion

#### 3.1. Thermal stability of the HCP materials

Fig. 2 shows thermogravimetric (TG) curves in air (a – c), in argon (d – f), and the corresponding differential thermogravimetric (DTG) curves in argon (g – i) for HCPs synthesised: I) from carbazole with different amounts of catalyst, II) from different precursors at a fixed amount of catalyst, and III) from carbazole with different ratios of GO.

The TG curves in air exhibit a similar behaviour for all samples and no change in the mass of the material is noticed below 533 K. A slight gain in weight is observed between 533 K and 673 K, which may be due to the oxidation of the HCPs, consistent with what has been observed in other studies [54,55]. Degradation of the HCPs in air takes place at temperatures above 673 K up to 873 – 923 K. The low residual mass (<4 wt%) observed at 1223 K in air could be explained by the remaining iron oxides from FeCl<sub>3</sub> (Fig. 2a, b and c). Under Ar atmosphere, the samples showed a different behaviour depending on the synthesis conditions, but a high thermal stability was observed and high residue yields (>63 wt%) at 1223 K were obtained in all cases (Fig. 2d, e and f). This high sta-

bility at high temperature, typically up to 673 K both in air and under Ar atmosphere, is in good agreement with the results reported for other HCPs in the literature [56–58] and is evidence of a high degree of crosslinking [58–60].

The specific temperatures at which weight losses take place can be better appreciated in the DTG curves (Fig. 2g, h and i). The first weight loss, observed for all HCPs (line 1 in the plots), occurs between 313 and about 413 K and could be attributed to the release of moisture and evaporation of some of the solvent remaining in the pore network [27,57,61]. In the case of carbazole-derived HCP a second weight loss (line 2 in the plots) takes place between 533 and 693 K and could be attributed to the loss of terminal hydroxymethyl groups that are bonded to a only one aromatic ring (i.e., dimethoxymethane – derived moieties that did not complete the cross-linking reaction) and also to the evaporation of molecules of carbazole (boiling point 630.7 K) that did not react and remained trapped in the porosity. Finally, the third weight loss (line 3 in the plots) occurs between 753 and 1113 K, with a maximum at 860 K, and it could be attributed to polymer degradation. An almost constant weight loss is observed for all three samples up to 1223 K, which could be assigned to aromatisation-condensation reactions, loss of chemical functions due to dehydrogenation reactions, among others, as reported in previous studies [62–64]. The yields at 1223 K on dry basis (calculated with respect to the mass at 423 K, after the first weight loss) were 70, 75 and 75 wt% for C1Fe2M2, C1Fe1M2 and C1Fe0.2 M2, respectively (Fig. 2d). Higher catalyst to monomer molar ratios produced a very fast polymerisation rate, with complete polymer formation within a few minutes after addition of the catalyst, which most probably led to the formation of a large number of shorter and more disorganised polymer chains. The latter could explain the lower carbonisation yield of the C1Fe2M2 sample compared to the other HCPs prepared

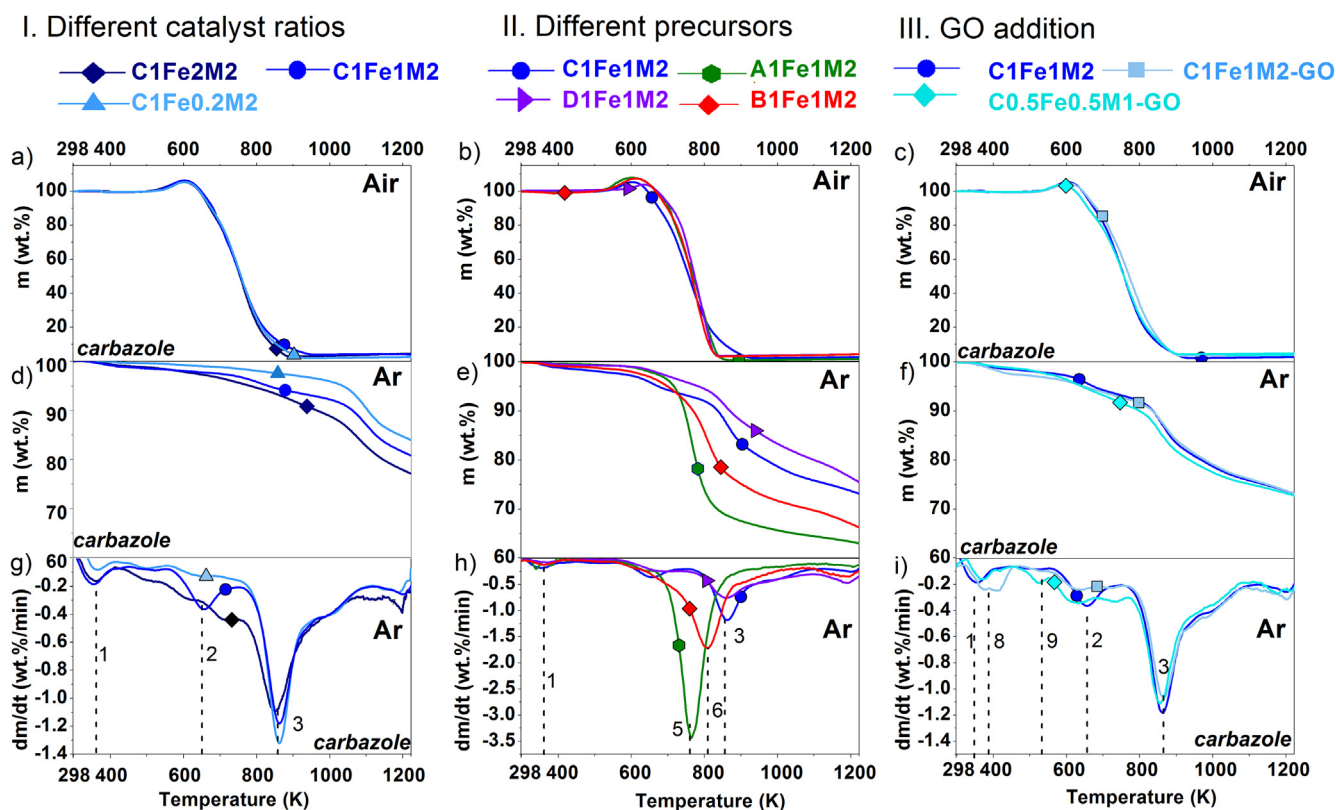


Fig. 2. TG in air and in Ar, and DTG in Ar for: I) the C-HCPs synthesised with different amounts of catalyst (C1Fe2M2, C1Fe1M2 and C1Fe0.2 M2) (a, d and g); II) HCPs synthesised from different precursors (C1Fe1M2, A1Fe1M2, D1Fe1M2, and B1Fe1M2) (b, e and h); and III) C-HCPs synthesised with different ratios of GO (C1Fe1M2, C1Fe1M2-GO, C0.5Fe0.5 M1-GO) (c, f and i).

with lower amounts of catalyst. Furthermore, although the yields on dry basis of samples C1Fe1M2 and C1Fe0.2 M2 are similar, the former loses less weight in the polymer degradation step (line 3). For this reason, we selected the precursor/ $\text{FeCl}_3$  molar ratio of 1:1 for the following experiments.

Fig. 2e and h shows the TG and DTG curves in Ar of HCPs prepared using different precursors and with a precursor/catalyst molar ratio of 1:1. The final yields at 1223 K on dry basis were 63, 67, 75, 76 wt% for samples A1Fe1M2, B1Fe1M2, C1Fe1M2 and D1Fe1M2, respectively. The thermal stability of the HCPs followed the same order. Thus, the temperature of the maximum weight loss rate of degradation step of these HCPs was 761 K for the anthracene-derived HCP (line 5 in Fig. 2h), 808 K for the benzene-derived one (line number 6) and 860 K for polymers prepared using carbazole and dibenzothiophene (line number 3). As discussed above, the higher the thermal stability of the materials, the greater the degree of crosslinking that can be expected from them [60]. The latter may be related to the different reactivity of these monomers in electrophilic aromatic substitution reactions. Carbazole and dibenzothiophene are  $\pi$ -electron donating aromatic compounds due to the unshared electron pair of their heteroatom, which substantially stabilises the cationic intermediate in the electrophilic aromatic substitution reaction, making these monomers more reactive [65]. In the case of anthracene, although it is slightly more reactive than benzene in the electrophilic aromatic substitution, because polymerisation takes place very rapidly once the catalyst is added, the greater steric hindrance of the former may lead to a lower degree of crosslinking in the final HCP [63].

Finally, Fig. 2f shows the thermal degradation of carbazole-based HCP synthesised in the presence of different GO ratios. No substantial change in the weight loss profile and in the final yield at 1223 K on dry basis (75 wt%) was observed when the TG measurement of the C1Fe1M2, C1Fe1M2-GO and C0.5Fe0.5 M1-GO samples was performed under Ar. Therefore, the addition of GO does not seem to affect the thermal stability of the HCPs, which may indicate that a similar degree of crosslinking was achieved and that the presence of GO did not significantly alter the reaction path. The only differences observed in the DTG curves (Fig. 2i) are between 373 and 573 K (lines 8 and 9, respectively) and could be attributed to the loss of adsorbed water and of labile oxygen-containing functional groups from GO, in good agreement with the literature [49,66,67].

### 3.2. Composition of the HCP materials

The oxygen, hydrogen, carbon, nitrogen and sulphur content of the HCPs and HCPs-GO, determined by elemental analysis, is reported in the supporting information (Table S1). High purity of the samples was observed, as >98.3 wt% was attributed to their expected elemental composition: O, H, C and the heteroatoms (N or S). The unknown composition of the remaining 1.7 wt% could be attributed to iron oxides, among others. The discrepancy between the final yield after complete calcination in air by TG analysis (<4 wt%) and the elemental analysis results can be ascribed to measurement errors, or to the fact that the latter technique is performed at a higher temperature (1973 K) than that of the TG technique (1223 K). Thus, it is likely that the ash composition differs between the two techniques.

The carbon and hydrogen contents of the materials were in the ranges of 76–88 and 3.5–5.0 wt%, respectively. Fig. 3a shows the heteroatom content of the HCPs and HCPs-GO. As expected, nitrogen (~6–7 wt%) and sulphur (~17 wt%) were found in the carbazole- and dibenzothiophene-derived HCPs, respectively. The oxygen content in the carbazole-derived HCPs was 12.7, 8.0 and 8.8 wt% for C1Fe2M2, C1Fe0.2 M2, and C1Fe1M2, respectively. As oxygen is sourced from the crosslinker (dimethoxymethane), a higher percentage of oxygen would indicate that the polymer network has a larger amount of incomplete crosslinks (in the form of methoxymethyl moieties), which in turn would be consistent with lower residue yields at 1223 K as seen by TG analysis under Ar (Fig. 2d). The oxygen content is therefore inversely related negatively correlated to the thermal stability of the samples.

The O/C and H/C atomic ratios for the HCPs, HCPs-GO and precursors used were plotted in a Van Krevelen-type diagram [68,69] (Fig. 3b), those of the monomers being calculated from their molecular formulae. The H/C atomic ratio of the HCPs and HCP-GO composites decreased significantly compared to their precursors, which is consistent with the formation of chemical crosslinks by Friedel-Crafts alkylation according to the literature [68].

In the series of HCPs prepared from different precursors, the oxygen content was 2.8, 8.1, 8.8 and 11.0 wt% for D1Fe1M2, B1Fe1M2, C1Fe1M2 and A1Fe1M2, respectively. This is consistent with their thermal stability, since samples with higher oxygen content could have a larger extent of incomplete crosslinks. Fig. 3b shows that the O/C ratio increased for the carbazole-

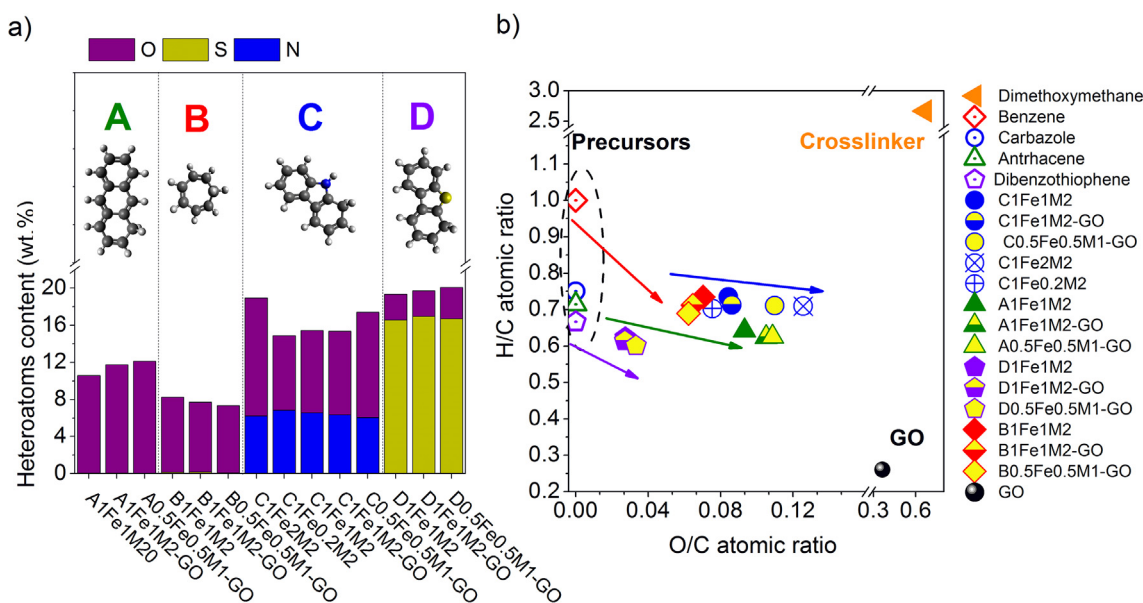


Fig. 3. a) Heteroatoms content of the HCPs and HCP-GO composites; b) Van Krevelen diagram for the precursors, HCP and HCP-GO materials.

dibenzothiophene- and anthracene-based HCPs when GO was incorporated, due to the high oxygen content of the GO added [68]. The O/C ratio was slightly reduced for the benzene-derived HCP when GO was added and this is tentatively attributed to experimental error. Further additions of GO, in the range of 0.05 to 1.00 g, showed that the O/C ratio increased with the amount of GO, in good agreement with other HCPs prepared from different precursors. The latter results, not presented here, will be the subject of a future study.

### 3.3. Morphology of the HCP materials

Fig. 4 shows SEM images of HCPs synthesised using carbazole as a precursor (C1Fe1M2) and their HCP-GO composites (C1Fe1M2-GO and C0.5Fe0.5 M1-GO). The materials synthesised without the addition of GO are largely obtained in the form of uniformly sized microspheres with diameters somewhat below 1  $\mu\text{m}$  (Fig. 4a), in good agreement with previous results reported elsewhere [22,70].

The addition of GO to the reaction medium at a relatively high reactants to GO ratio (i.e., sample C1Fe1M2-GO) led to the formation of more polydisperse HCP spheres, with diameters typically ranging between 0.1 and 1.5  $\mu\text{m}$  (Fig. 4b). When the reactants to GO ratio is decreased (sample C0.5Fe0.5 M1-GO, Fig. 4c), the polymer spheres become again more uniform in size, but their diameter is smaller than that of their GO-free counterpart (typically somewhat below 0.5  $\mu\text{m}$ ). While it is obvious that the presence

of GO sheets has an impact on the morphological characteristics of the HCP products, the origin of such an effect is not immediately apparent. As a plausible explanation, we note that in the presence of GO, a spatially confined reaction volume formed by neighbouring GO sheets must be generated throughout the synthesis medium. In these confined volumes, the supply of precursor to generate HCP spheres is expected to be limited to an extent determined by the actual size of these confined volumes, which in turn are defined by the distance between neighbouring GO sheets. Because the sheets cannot be expected to be evenly spaced in the reaction solvent, and thus confined reaction volumes of different sizes are present, HCP spheres of different sizes will be generated (e.g. sample C1Fe1M2-GO). If the total amount of precursors is reduced (sample C0.5Fe0.5 M1-GO), their supply will be limited even in the largest confined volumes, so that the size of the resulting HCP spheres should be drastically decreased, as was actually observed.

### 3.4. Porous texture of the HCP materials

Fig. 5 and Figure S1 show the results of pore texture characterisation of the HCPs prepared from different precursors (A1Fe1M2, B1Fe1M2, C1Fe1M2 and D1Fe1M2) and using different amounts of catalyst (C1Fe2M2, C1Fe1M2 and C1Fe0.2 M2). The derived pore texture parameters are presented in the supporting information (Table S2). The shape of the  $\text{N}_2$  isotherms remained the same when

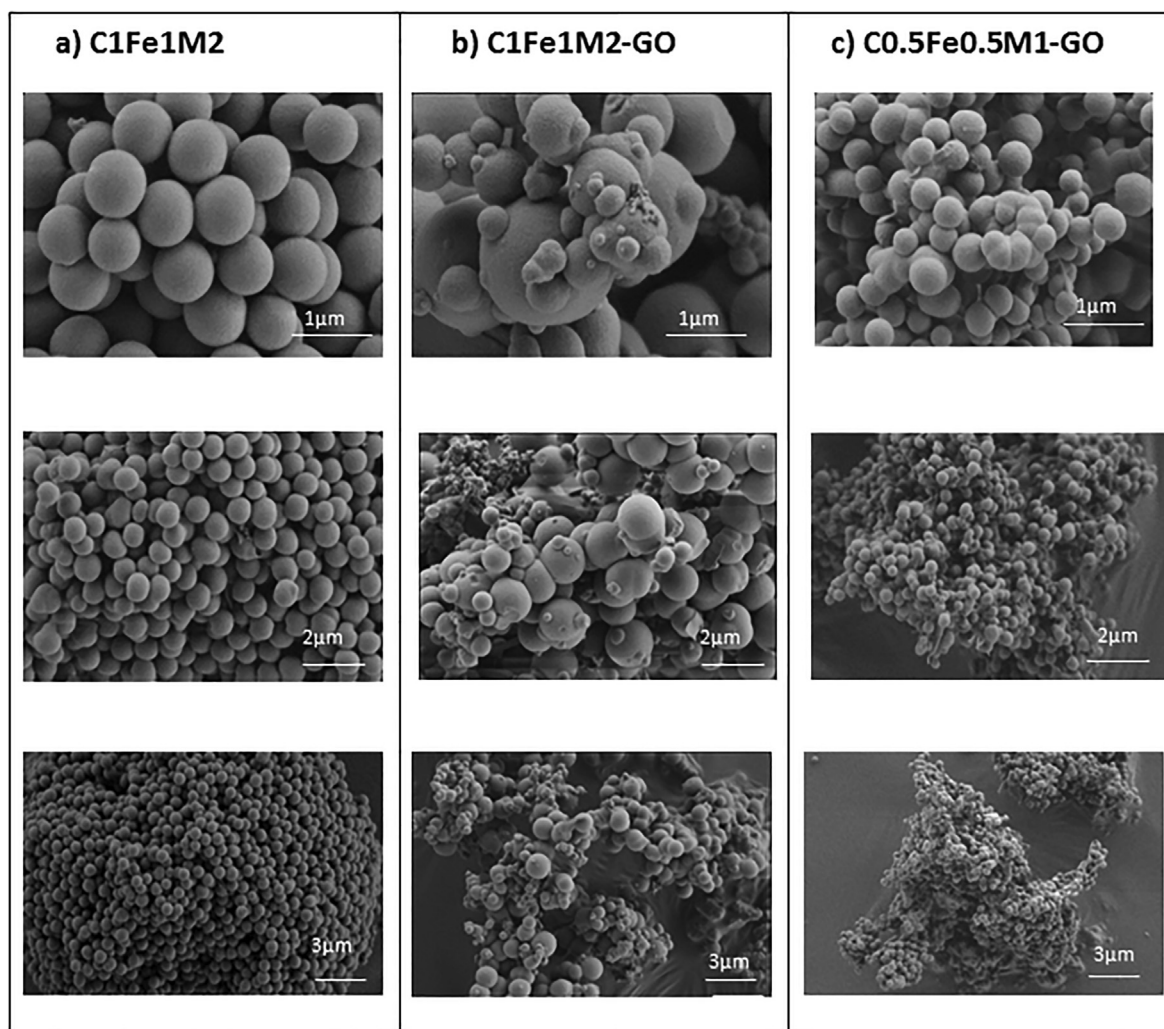
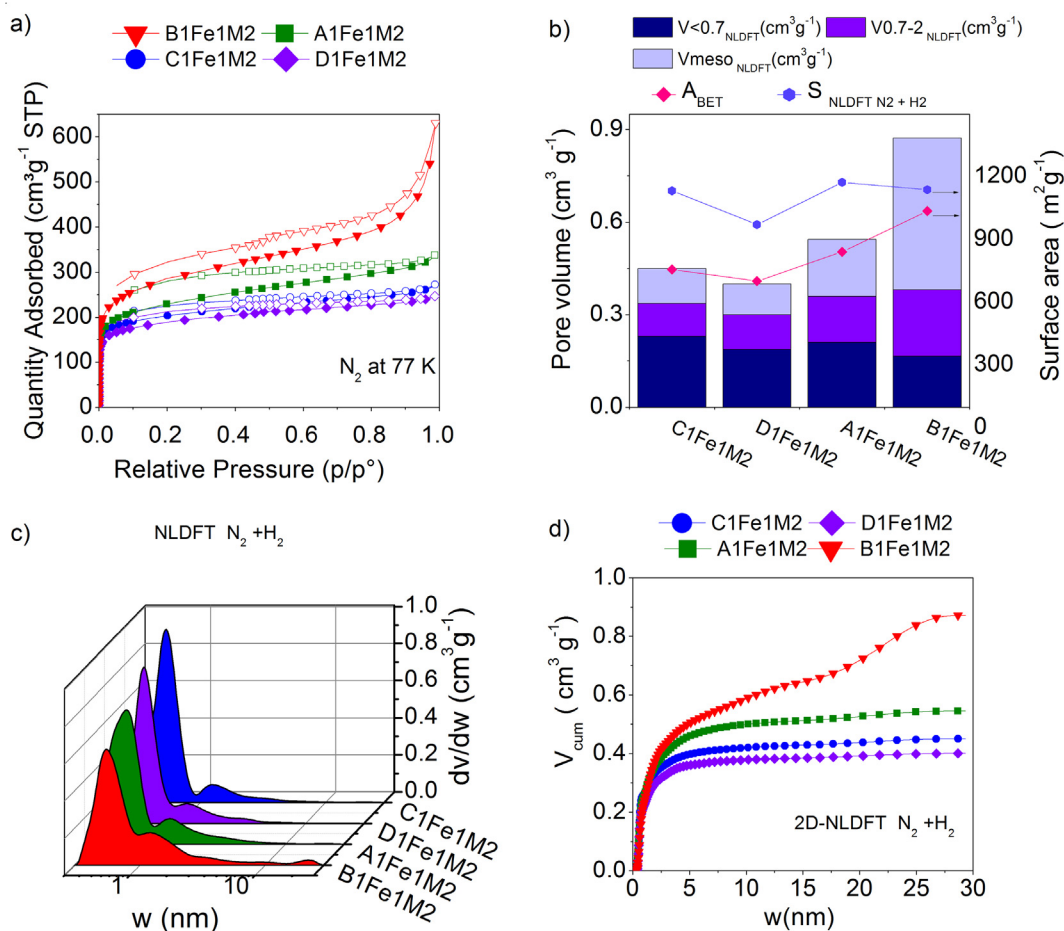


Fig. 4. SEM images of carbazole-derived HCPs at different magnifications: a) C1Fe1M2, b) C1Fe1M2-GO and c) C0.5Fe0.5M1-GO.



**Fig. 5.** Textural characteristics of A1Fe1M2, B1Fe1M2, C1Fe1M2 and D1Fe1M2: a) N<sub>2</sub> adsorption–desorption at 77 K (full and empty symbols stand for adsorption and desorption, respectively); b) Surface areas  $A_{\text{BET}}$  and  $S_{\text{NLDFT N}_2\text{-H}_2}$ , and pore volumes (ultramicropores (<0.7 nm), supermicropores (0.7–2 nm) and mesopores (2–50 nm)) deduced from NLDFT applied to N<sub>2</sub> + H<sub>2</sub> isotherms; c) PSDs from the NLDFT 2D fitting of both N<sub>2</sub> and H<sub>2</sub> isotherms; d) cumulative pore volumes from the same N<sub>2</sub>-H<sub>2</sub> NLDFT 2D fitting.

the amount of catalyst was changed for the carbazole-based HCPs (Figure S1). A more developed porous texture was observed in sample C1Fe1M2 compared to C1Fe2M2 and C1Fe0.2 M2. For carbazole-based HCPs,  $A_{\text{BET}}$  and  $S_{\text{NLDFT}}$  ranged from 695 to 757 m<sup>2</sup> g<sup>-1</sup> and from 834 to 1132 m<sup>2</sup> g<sup>-1</sup>, respectively, with the highest values being measured for C1Fe1M2 due to its higher percentage of ultramicropores (>51 %) and supermicropores (>24 %) (Figure S1). The total pore volume as well as the mesopore and micropore volumes increased in the order C1Fe2M2 < C1Fe0.2 M2 < C1Fe1M2, which is also the order of the increase in the degree of crosslinking observed by TG analysis (Fig. 2).

Fig. 5a shows the N<sub>2</sub> adsorption–desorption isotherms at 77 K for the HCPs prepared from different precursors. In agreement with other studies [71–73], the hysteresis cycle did not close at low pressures in all cases, which can be attributed to swelling [72,74] due to some elasticity of the HCPs or to diffusion limitations in the narrow micropores [71]. In the first case, it is assumed that the HCPs have a flexible structure, which can lead to the formation of new pores or the enlargement of pre-existing pores when the amount of gas inside them increases (swelling) [75]. Therefore a dual-mode sorption occurs: once the pre-existing pores are filled prior to swelling, the latter takes place and produces an additional adsorption, which is proportional to the pressure [72,74]. The second possibility to explain the phenomenon is to consider that there are diffusional problems associated with the microporous morphology due to restricted filling of pre-existing pores [71].

The carbazole and dibenzothiophene-based HCPs (C1Fe1M2 and D1Fe1M2) exhibited type Ib isotherms, according to the IUPAC classification [76] (Fig. 5a), indicating well developed microporosity with ultramicropores but also a high percentage of supermicropores (Fig. 5b and c). The percentage of micropores was 75 % for C1Fe1M2 and D1Fe1M2, of which approximately two thirds were ultramicropores (Fig. 5b). The high amount of micropores in C1Fe1M2 and D1Fe1M2 samples was consistent with their high thermal stability (Fig. 2e) which, as seen previously, is an indication of the degree of crosslinking [60]. The anthracene-derived HCP sample, A1Fe1M2, also showed well-developed microporosity (67 %) but its corresponding N<sub>2</sub> adsorption isotherm increased almost linearly at medium and high relative pressures. In addition, a large hysteresis at low pressure is observed (Fig. 5a). The benzene-derived HCP sample, B1Fe1M2, showed a combined type Ib + type IV isotherm shape with a non-reversible H4 hysteresis loop type, indicating a large mesopore fraction (Fig. 5a). Its percentage of microporous volume was only 44 %, of which more than half corresponded to supermicropores (Fig. 5b). The high fraction of mesoporous volume in B1Fe1M2 is an unexpected but consistently observed result, which will be examined thoroughly in future studies. The percentage of mesoporous volume was 24, 25, 35 and 56 % for C1Fe1M2, D1Fe1M2, A1Fe1M2 and B1Fe1M2, respectively.

Fig. 5c and d show the PSDs and the cumulative pore volumes, respectively, of samples A1Fe1M2, B1Fe1M2, C1Fe1M2 and

D1Fe1M2. All samples presented a bimodal PSD with a first dominant peak in the range of 0.3–0.9 nm and a second peak in the range of 0.9–5.7 nm (Fig. 5c). The average micropore and pore sizes were in the ranges of 0.72–0.89 and 2.41–8.09 nm, respectively (Table S2) and increased in the order C1Fe1M2 < D1Fe1M2 < A1Fe1M2 < B1Fe1M2. Figure S2 shows the CO<sub>2</sub> isotherms obtained at 273 K. The CO<sub>2</sub> uptake decreased in the order C1Fe1M2 > A1Fe1M2 > B1Fe1M2 > D1Fe1M2. As CO<sub>2</sub> adsorption gives a good assessment of pores smaller than 1 nm, the total CO<sub>2</sub> adsorption correlates quite well with the ultramicropore volume (0.23, 0.21, 0.16, 0.19 cm<sup>3</sup> g<sup>-1</sup> for C1Fe1M2, A1Fe1M2, B1Fe1M2 and D1Fe1M, respectively) except for B1Fe1M2 that has developed supermicroporosity (i.e., pore diameters between 0.7 and 2 nm). Furthermore, this could be attributed to the swelling of the B1Fe1M2 sample in the presence of CO<sub>2</sub>, as reported by Lee et al. [77].

The values of  $A_{\text{BET}}$  were between 701 and 1036 m<sup>2</sup> g<sup>-1</sup> and those of  $S_{\text{NLDFT}}$  between 971 and 1137 m<sup>2</sup> g<sup>-1</sup> (Fig. 5b). The  $A_{\text{BET}}$  values of the HCPs are in line with those reported in the literature [18,19,78]. Higher specific surface areas were obtained when the 2D-NLDFT-HS method was employed compared to the BET method (see Table S2 and Table S3 in the Supporting Information). This can be attributed to a better quantification of the narrowest micropores by the 2D-NLDFT-HS method, as it was achieved by simultaneously fitting N<sub>2</sub> and either CO<sub>2</sub> or H<sub>2</sub> adsorption data [53,79–84]. Although the kinetic diameters of N<sub>2</sub> and CO<sub>2</sub> are similar (0.36 and 0.33 nm, respectively), CO<sub>2</sub> physisorption is a process that occurs at a much higher temperature (273 K) compared than N<sub>2</sub> physisorption (77 K). Consequently, CO<sub>2</sub> diffuses much faster than N<sub>2</sub> and is adsorbed in pores where N<sub>2</sub> cannot enter within the set equilibrium times [51,85]. The other approach proposed to overcome the problems of N<sub>2</sub> diffusion at 77 K into the micropores is the use of H<sub>2</sub> adsorption experiments [83]. Having a smaller kinetic diameter (0.29 nm), H<sub>2</sub> can access to the narrowest pores. However, higher specific surface areas and supermicropore volumes were measured with the N<sub>2</sub>-CO<sub>2</sub> pair, which could be related to specific interactions between CO<sub>2</sub> and HCPs [86,87], resulting in the swelling of HCPs [72,77].

Fig. 6 reports results of the textural characterisation of the third series of materials, and specifically, when GO was added to the benzene-based HCPs. Fig. 6a shows that the shape of the N<sub>2</sub> isotherms was only slightly modified by the addition of GO and that this change was limited to a reduction in adsorbed volume at  $p/p_0 < 0.1$ , whereas in the  $p/p_0$  range of 0.1 to 0.6, a slightly steeper slope was observed. These changes indicate a reduction in micropore volume and an increase in mesopore volume upon addition of GO. Figure S3 shows the N<sub>2</sub> adsorption-desorption isotherms for the HCPs prepared from different precursors after addition of GO. Anthracene-based HCPs showed similar trends to those of benzene-derived materials, while HCPs derived from carbazole and dibenzothiophene only showed a reduction in microporosity without noticeable change in mesoporosity. CO<sub>2</sub> and H<sub>2</sub> uptakes also decreased when GO was added (Fig. 6b, c and Figure S4), indicating a reduction in pores below 1 nm. In general, the synthesised materials exhibited a minor change in specific surface area, as the variations of  $A_{\text{BET}}$  and  $S_{\text{NLDFT, N}_2\text{-H}_2}$  were about 10 % and 15%, respectively, when GO was incorporated into the polymerisation medium (Table S2 and Table S3).

The PSDs for all samples and hydrogen isotherms at 77 K and up to 0.1 MPa are shown in Figure S6 and Figure S5, respectively. All the materials exhibited a bimodal PSD (Figure S5), although the average micropore size increased slightly (<6%) for all precursors after addition of GO. This finding is in good agreement with the changes observed in the N<sub>2</sub> and CO<sub>2</sub> isotherms.

Minor changes in the specific surface area and shape of the N<sub>2</sub> isotherms at 77 K were also reported by Castaldo et al [46] when

GO was added to the polymerisation medium of styrene-based HCPs. These HCP composites exhibited values of  $A_{\text{BET}}$  in the range of 170–1910 m<sup>2</sup> g<sup>-1</sup> with a slight increase in micropore fraction (3–14 %) and a reduction in total pore volume (10–16 %) when GO was incorporated. Their change in textural properties was attributed to the increase in crosslinking reactions through the interaction of GO with the functional groups in the styrene-based materials. However, because the textural characterisation was only performed using N<sub>2</sub> adsorption data at 77 K, it is possible that GO-induced changes in micropore volume were not properly assessed. Although the textural properties of the materials synthesised here are similar to those reported in the literature [45,46], the addition of the GO using the knitting method followed in this study has the advantage of being less time-consuming as it is a one-step reaction that does not require prior pre-polymerisation.

### 3.5. H<sub>2</sub> and CO<sub>2</sub> storage capacities at atmospheric pressure

Most studies provide storage capacities per gram of sorbent, but storage capacities per unit volume are a much more significant parameter when considering practical applications [10,88]. The tapped and skeletal densities of the samples are reported in Table S4. Figure S7a shows the tapped density of the samples before and after addition of GO. Carbazole- and benzene-based HCPs showed an increase in tapped density upon addition of GO, but no clear trend was observed with the other two precursors studied here.

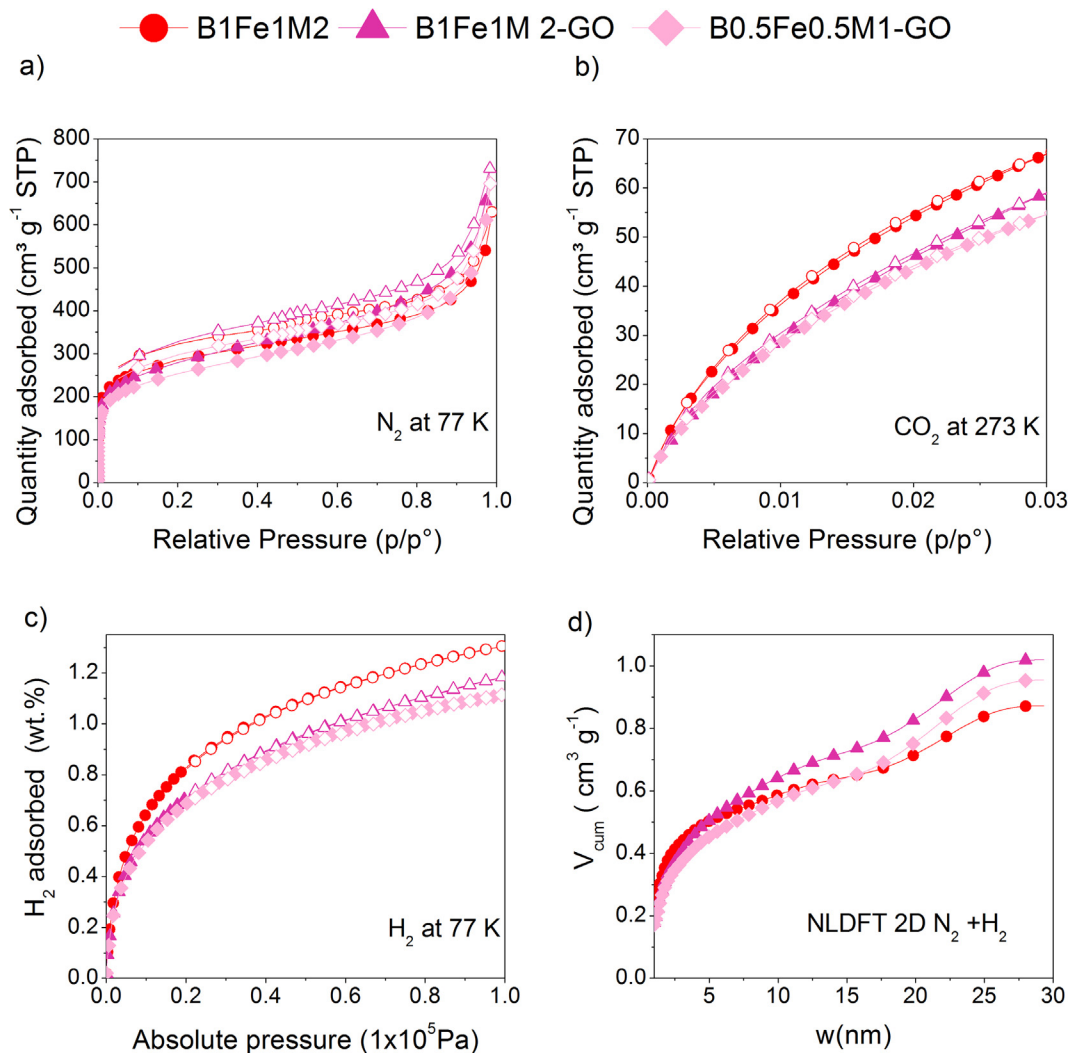
Fig. 7a shows that the hydrogen uptake on gravimetric basis at 77 K and 0.1 MPa follows a linear relationship when it is fitted through the origin at (0,0) with  $S_{\text{NLDFT, N}_2\text{-H}_2}$  ( $R^2 = 0.99$ ), whereas a lower  $R^2$  of 0.78 was determined when the hydrogen uptake was plotted as a function of  $A_{\text{BET}}$  (Figure S7). This shows that the surface area calculated by the BET method from the N<sub>2</sub> isotherms did not correctly characterise the porosity involved in H<sub>2</sub> adsorption. However, by simultaneously combining the N<sub>2</sub> and H<sub>2</sub> isotherms using the NLDFT method, the porosity where hydrogen is adsorbed (i.e., the narrowest micropores) was adequately determined.

Fig. 7b shows the H<sub>2</sub> volumetric uptake capacities as a function of  $S_{\text{NLDFT, N}_2\text{-H}_2}$  for all samples. Although B1Fe1M2 has a higher H<sub>2</sub> uptake on a gravimetric basis than C1Fe1M2, the latter sample adsorbed 1.4 times more H<sub>2</sub> when storage capacities were reported on a volumetric basis due to its much higher tapped density (0.13 g cm<sup>-3</sup>) compared to that of B1Fe1M2 (0.06 g cm<sup>-3</sup>). The sample with the highest volumetric H<sub>2</sub> uptake was C1Fe1M2-GO (3.3 g L<sup>-1</sup>).

Fig. 8 shows the H<sub>2</sub> and CO<sub>2</sub> uptakes at 77 K and 273 K, respectively, both at 0.1 MPa, as a function of  $A_{\text{BET}}$  for our materials (see the corresponding data in Table S4) and other HCPs reported in the literature [18,20–22,30–39,89–92] (see data in Table S5). In the latter Table, the synthesis conditions and textural parameters are also given. Although better fitting coefficients were obtained when the H<sub>2</sub> uptake was plotted against  $S_{\text{NLDFT, N}_2\text{-H}_2}$ ,  $A_{\text{BET}}$  was used to make a more representative comparison with the data reported in the literature. Our materials showed average H<sub>2</sub> and CO<sub>2</sub> capacities and a linear trend similar to that shown by materials reported in the literature.

### 3.6. High-pressure H<sub>2</sub> adsorption

Since benzene-derived HCPs showed the highest  $V_T$  (see Fig. 5d and Tables S2 and S3) and H<sub>2</sub> uptake is directly proportional to  $V_T$  at high pressure [93], samples B1Fe1M2 and B1Fe1M2-GO were selected for studying their high-pressure hydrogen adsorption. Fig. 9a shows the H<sub>2</sub> adsorption at 77 K and at pressures up to 14 MPa on sample B1Fe1M2, where the repeatability of the mea-



**Fig. 6.** Textural characteristics of the benzene-derived HCP samples: a) N<sub>2</sub> adsorption–desorption isotherms at 77 K; b) CO<sub>2</sub> adsorption–desorption isotherms at 273 K; c) H<sub>2</sub> adsorption isotherms at 77 K and up to 0.1 MPa; d) cumulative pore volume from the NLDFT fitting of N<sub>2</sub> and H<sub>2</sub> isotherms. In a), b) and c), full and empty symbols stand for adsorption and desorption, respectively.

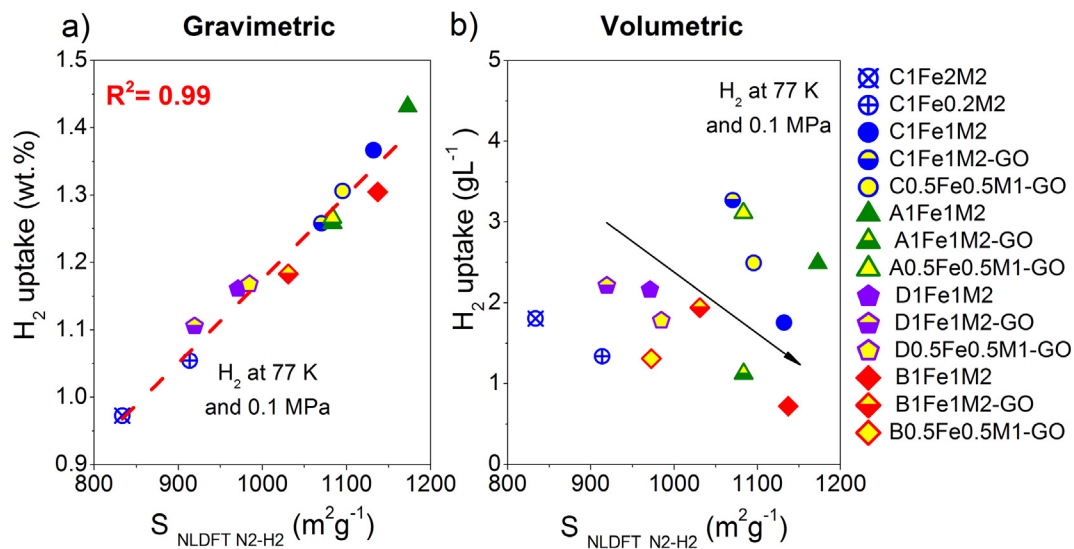


**Fig. 7.** a) H<sub>2</sub> uptake per mass (wt. %) and per volume (g L<sup>-1</sup>) as a function of the surface area S<sub>NLDFT N<sub>2</sub>-H<sub>2</sub>, at 77 K and 0.1 MPa.</sub>

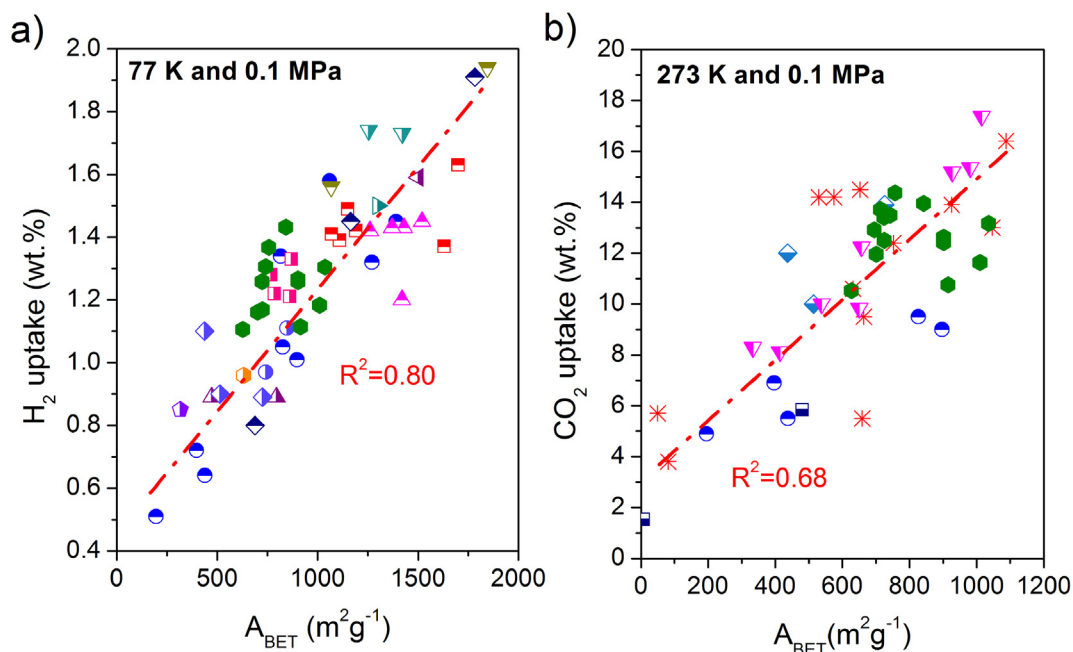


**Fig. 8.** a)  $H_2$  uptake at 77 K and 0.1 MPa; and b) uptake at 273 K and 0.1 MPa of our materials (green hexagons) and other materials reported in the literature [20], [18], [21], [34], [32], [33], [30], [31], [35], [36], [92], [38], [89], [37], [22], [39], [90], [91]. (For interpretation of the references to colour in this figure legend, the reader is referred to the web version of this article.)

surement was studied. For this purpose, we carried out 3 consecutive adsorption–desorption measurements with a 12 h outgassing step under secondary vacuum and heating at 333 K for the first adsorption, and without heating for the outgassing before the following consecutive isotherms. The isotherms were thus labelled 12 h-1, 12 h-2 and 12 h-3, i.e., in increasing numerical order as they were measured. Hydrogen adsorption was repeatable with an average variation of 3% over a pressure range of 0.1–10 MPa. However, differences from one isotherm to another were found and increased up to 13% in the pressure range between 10 and 14 MPa.

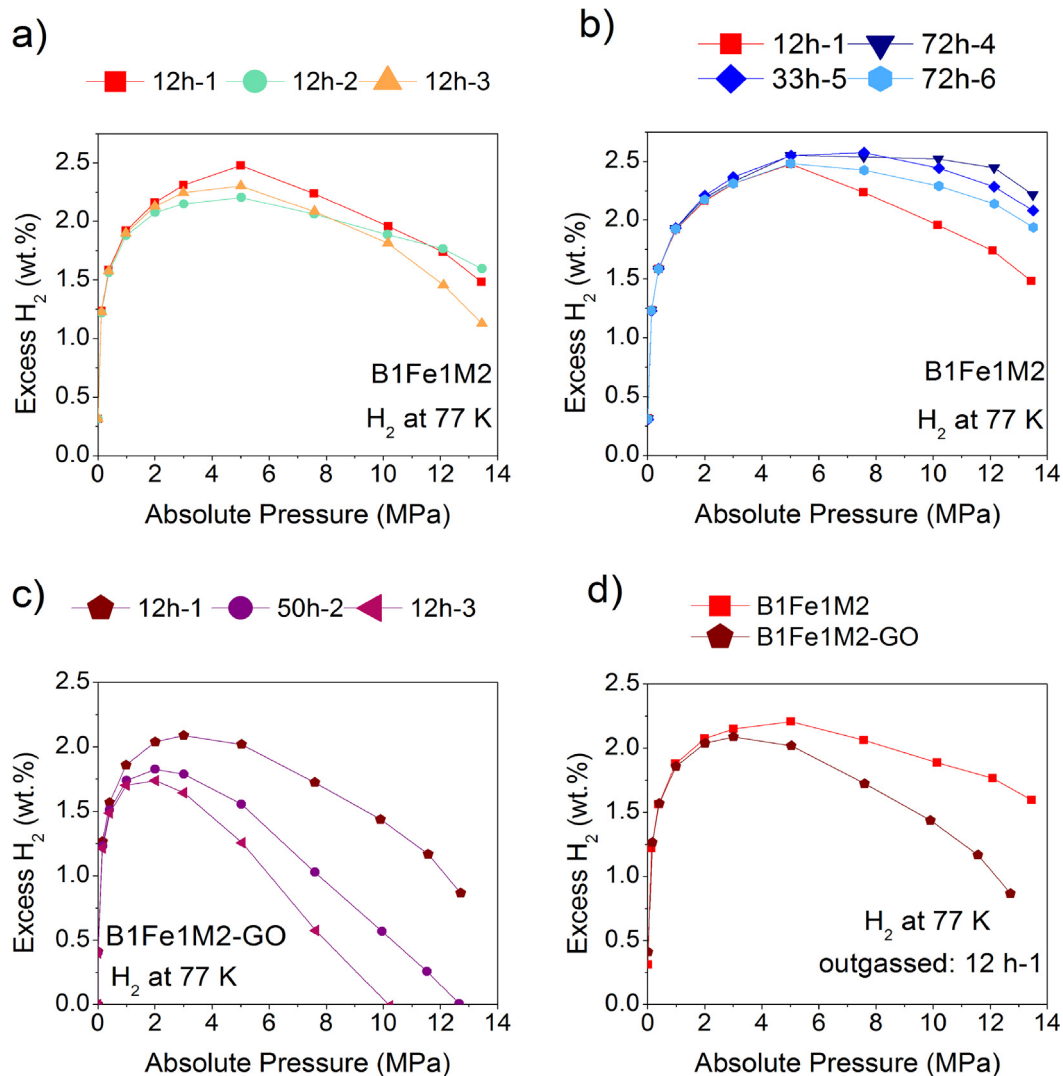
Fig. 9b compares the first of the previous isotherms with those obtained after outgassing for 72 h (isotherm labelled 72 h-4), 33 h (labelled 33 h-5) and 72 h (labelled 72 h-6). Higher  $H_2$  uptake was observed when longer outgassing times were used and thus the measured capacity for the 72 h-4 sample is higher than that of samples outgassed for 12 h (12 h-1, 12 h-2 or 12 h-3). This could be attributed to swelling [72,74], as the pores can indeed be enlarged during outgassing under secondary vacuum due to the elasticity of the HCPs. An argument in favour of swelling is that the changes occur at pressures above 4 MPa. If the longer outgassing time had an effect on the better degassing of very narrow pores [71], differences would have been observed at pressures below 4 MPa [94]. Figure S8a–b shows a zoomed-in capture confirming that minor differences in hydrogen adsorption are observed at pressures below 4 MPa. We can also observe that, after the first outgassing for 72 h, the hydrogen capacities decrease in the order 72 h-4 > 33 h-5 > 72 h-6. Therefore, successive outgassing–adsorption–desorption cycles would irreversibly modify the HCPs.

Fig. 9c shows three consecutive  $H_2$  adsorption–desorption isotherms at 77 K in the pressure range 0.1–14 MPa on B1Fe1M2-GO when the same sample was outgassed firstly for 12 h before performing the first adsorption–desorption cycle (12 h-1), for 50 h before doing the second adsorption–desorption cycle (50 h-2), and for 12 h before doing the third adsorption–desorption cycle (12 h-3). A significant reduction in hydrogen uptake was observed

in the second cycle after 50 h of outgassing, and the hydrogen capacity was further reduced in the third adsorption–desorption cycle (12 h-3). The addition of GO appears to have a detrimental effect on the mechanical properties of the HCPs and on the hydrogen storage capacities of the materials when expressed on a mass basis, as the  $H_2$  excess uptakes were 2.1 and 2.0 wt% for B1FeM2 and B1FeM2-GO, respectively, in the first adsorption–desorption cycle at 4 MPa and 77 K. However, when reported on a volumetric basis, the excess  $H_2$  uptakes were 1.2 and 3.3 g L<sup>-1</sup> for B1FeM2 and B1FeM2-GO, respectively. Therefore, the addition of GO seems to be beneficial in modifying the morphology of the composites, allowing a higher tapped density and ultimately a higher  $H_2$  uptake relative to the sample volume. This clearly demonstrates that, for practical applications, volumetric capacity and not gravimetric capacity should be considered, and that the use of mass capacities alone can lead to misleading conclusions.

Fig. 10a, b and Figure S9 show the textural characterisation of samples B1FeM2 and B1FeM2-GO before and after  $H_2$  adsorption at high pressure. The  $N_2$  isotherms of the samples before and after  $H_2$  adsorption at high pressure reveal the change in PSD of the samples (Figure S9a–b). For sample B1Fe1M2 (Figure S9a), the total  $N_2$  adsorbed (at  $p/p_0 = 0.97$ ) remained almost the same (8.4% increase) but changes are observed in the shape of the  $N_2$  isotherm. For  $p/p_0 < 0.7$ , the amount of  $N_2$  adsorbed decreased whereas for  $p/p_0 > 0.7$ , it increased compared to the sample before  $H_2$  adsorption at high pressure. This is evidence of a reduction in the narrowest pores and an increase in the widest ones after  $H_2$  adsorption at high pressure. In line with these results, a reduction in  $H_2$  uptake at low pressure (up to 0.1 MPa) was observed when comparing the data after and before subjecting the sample B1Fe1M2 to  $H_2$  at high pressure (Figure S9c). This could be due to the merging of micropores into larger pores that are less prone to overlapping adsorption potentials of their pore walls.

The PSDs of B1Fe1M2 obtained from the 2D NLDFT before and after high-pressure cycles of  $H_2$  adsorption are plotted in Figure S9e. The ultramicroporous, supermicroporous and mesoporous volumes after high-pressure  $H_2$  adsorption were 0.14, 0.18 and



**Fig. 9.** Hydrogen adsorption at 77 K, for pressures between 0.1 and 14 MPa, for the samples: a) B1Fe1M2 after 12 h outgassing; b) B1Fe1M2 after 12, 72, 33 and 72 h outgassing; c) B1Fe1M2-GO after 12, 50 and 12 h outgassing; d) B1Fe1M2 and B1Fe1M2-GO after the first 12 h outgassing.

0.61 cm<sup>3</sup> g<sup>-1</sup>, respectively. This implies a reduction of 13.9 and 14.7 % in the ultramicroporous and supermicroporous domain compared to the pristine sample, in good agreement with previous results. On the contrary, an increase of 25 % was observed in the mesoporous volume, and the total cumulated volume was increased by 8 %.

Figure S9b shows the N<sub>2</sub> adsorption–desorption isotherms on B1Fe1M2-GO before and after high-pressure cycles of H<sub>2</sub> adsorption. No shape changes were observed, except for a reduction in the amount of adsorbed gas over the entire  $p/p_0$  range. In good agreement with these results, a reduction in H<sub>2</sub> uptake at low pressure (up to 0.1 MPa) was observed in Figure S9d when comparing the B1Fe1M2-GO sample before and after high-pressure cycles of H<sub>2</sub> adsorption. Figure S9f shows the corresponding PSDs, from which we calculated that the ultramicroporous, supermicroporous and mesoporous volumes were reduced by 5, 15 and 7 %, respectively, with a 9 % reduction in total pore volume (Figure S9b). After the H<sub>2</sub> compression cycles performed on the B1Fe1M2 and B1Fe1M2-GO samples, a reduction of 10 and 20 % was observed in their  $A_{\text{BET}}$  values, and 12 and 5 % in their  $S_{\text{NLDFT N}_2\text{-H}_2}$  values, respectively.

For comparison, Fig. 10b shows the H<sub>2</sub> uptake for different HCPs from the literature at 77 K and in a pressure range of 1–4 MPa. The

colours purple and orange were used to represent absolute [40,42,77,95] and excess [31,41,43,96] hydrogen uptakes, respectively. Solid symbols indicate HCPs and HCP-composites while empty symbols represent activated carbons (ACs) derived from HCPs. The plotted data are shown in Table S6. So far, the reported hydrogen excess adsorption capacity at 77 K and high pressure are between 1.4 and 2.3 wt% and reaches 3.7 wt% of absolute adsorption capacity for HCPs and their composites with specific surface areas between 760 and 1904 m<sup>2</sup> g<sup>-1</sup> (Fig. 10b). The current record of H<sub>2</sub> absolute uptake in HCPs is 3.7 wt% at 77 K and 1.5 MPa for an HCP synthesised by self-condensation of bischloromethyl monomers [42]. At high pressure, hydrogen uptake in HCPs and HCP-derived ACs increases linearly with  $A_{\text{BET}}$  ( $R^2 = 0.90$ ) as observed for other porous materials [12,13]. H<sub>2</sub> adsorption on porous materials at high pressure and cryogenic conditions follows the so-called Chahine rule of thumb [97], which enounces that the H<sub>2</sub> uptake increases at a rate of 1 wt. % per 500 m<sup>2</sup> g<sup>-1</sup> of BET surface area. In Fig. 10b, it is observed that for HCPs with low surface areas, the H<sub>2</sub> uptakes are higher than expected for their  $A_{\text{BET}}$  according to the Chahine rule (black dashed line). This could be attributed to the well-known underestimation of the specific surface area of HCPs. As discussed in section 3.4, the BET theory underestimates the specific area regarding the narrowest pores (<0.7 nm) [51,85].

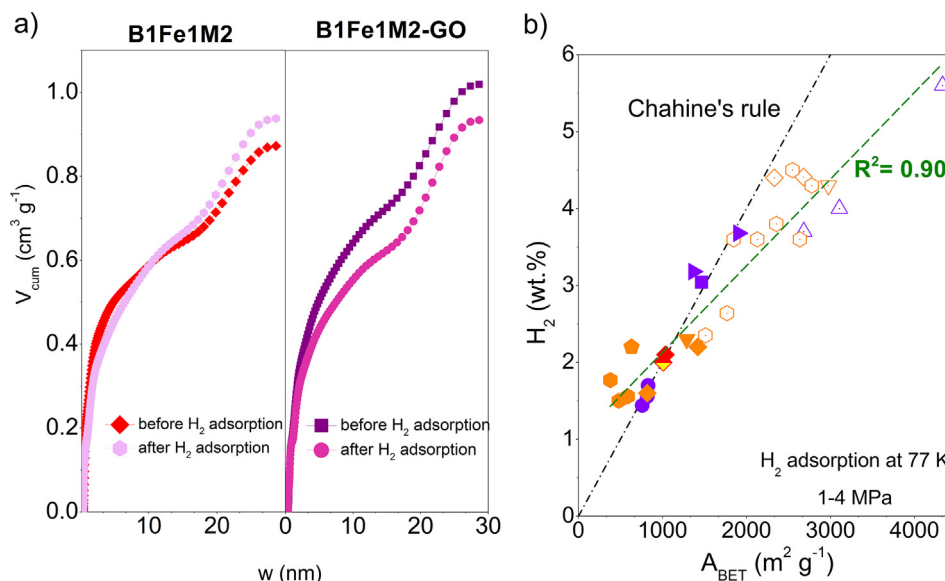


**Fig. 10.** a) Cumulated pore volumes  $V_{cum}$  (cm<sup>3</sup> g<sup>-1</sup>) for samples B1Fe1M2 and B1Fe1M2-GO before and after high-pressure cycles of H<sub>2</sub> adsorption; b) comparison of the obtained excess H<sub>2</sub> uptakes for samples B1Fe1M2 (◆) and B1Fe1M2-GO (◇) and the data reported from the literature at 77 K in the pressure range 1–4 MPa (■ [40], ● [95], ▲ [77], ▼ [42], ▽ [41], ◆ [31], ◇ [43], ○ [96]). Full and empty symbols indicate HCPs and activated carbons (ACs) synthesised from HCPs, respectively. Absolute and excess uptakes from the literature are plotted in purple and orange, respectively. (For interpretation of the references to colour in this figure legend, the reader is referred to the web version of this article.)

Therefore, a better correlation of the H<sub>2</sub> uptake at 77 K and high pressures with the  $S_{NLDFT\ N_2-H_2}$  could be expected, but  $S_{NLDFT\ N_2-H_2}$  data are not available in the literature. Indeed, we observed here a better correlation with the H<sub>2</sub> uptake at atmospheric pressure and 77 K with the  $S_{NLDFT\ N_2-H_2}$  ( $R^2 = 0.99$ ) than with  $A_{BET}$  ( $R^2 = 0.78$ ) (see section 3.5). Furthermore, the HCP-derived ACs show lower uptakes than expected for their  $A_{BET}$  according to the Chahine's rule. This is due to the fact that the BET theory overestimates the surface area of ACs having a large fraction of supermicropores (0.7–2 nm), since N<sub>2</sub> uptake proceeds by pore filling and not by monolayer adsorption [82].

Deformation of HCPs at high pressure (>4 MPa) has not been reported previously in the literature and this could be due to the fact that H<sub>2</sub> adsorption–desorption isotherms were mainly performed up to moderate pressures: up to 1–1.5 MPa [42,77,95], 2 MPa [43,96] or 3 MPa [31], and no cycling has been reported. As far as we know, there is only one study where higher pressures (10 MPa), close to those used in this study (14 MPa), have been used but no cycling was reported [41]. When cycling of H<sub>2</sub> isotherms has been reported, adsorption has been carried at lower pressures (1–1.5 MPa) where the irreversibility of the phenomenon is not apparent [40], as it also occurs in our case (see our high-pressure isotherm up to 1.5 MPa in Fig. 9).

For overcoming mechanical flexibility issues of HCPs and further develop their specific surface area, some studies proposed to chemically activate them with KOH [31,41–43,77,96]. The resulting ACs exhibited  $A_{BET}$  in the range of 1511–4334 m<sup>2</sup> g<sup>-1</sup> and consequently led to higher H<sub>2</sub> uptakes, from 2.3 to 4.5 wt% (excess) or 5.6 wt% (absolute adsorption), which are also shown in Fig. 10b. The reader should note that these hyperporous carbons, as they have been termed [77], are not fundamentally different from other ACs prepared from coals of different ranks or biomass by-products leading to H<sub>2</sub> uptakes as high as 6.6 wt% (at  $A_{BET}$  in the range of 2451–3451 m<sup>2</sup> g<sup>-1</sup>) [98–101]. Indeed, the synthesis of ACs from renewable precursors, such as agriculture by-products, would be cheaper and more environmentally friendly than the synthesis of equivalent materials from HCPs. The results obtained in the present study lead us to question the applicability of HCPs, their com-

posites and their derived ACs for high-pressure hydrogen adsorption.

#### 4. Conclusions

We have successfully synthesised hyper-crosslinked polymers (HCPs) by the Friedel-Crafts reaction using carbazole, anthracene, dibenzothiophene and benzene as precursors and dimethoxymethane as crosslinker. When graphene oxide (GO) was added to the HCPs during the syntheses, a change in their morphology as well as an increase in the tapped density in the resulting HCP-GO composites were observed. H<sub>2</sub> adsorption followed Chahine's rule for all materials, and the materials with the highest specific surface areas achieved the highest hydrogen storage capacities. However, when volumetric capacities were taken into account, which is necessary for practical applications, materials with lower  $A_{BET}$  outperformed those with higher  $A_{BET}$ . After H<sub>2</sub> adsorption at 14 MPa, irreversible changes in the porous texture of HCPs and HCP-GO composites were observed for the first time, and this produced a gradual decrease of the H<sub>2</sub> storage capacity with cycling. This study therefore shows that HCPs and HCP-GO composites cannot be used for high-pressure hydrogen adsorption. Although their use to produce high surface area-activated carbons has been proposed, we consider that the use of biomass by-products or coals as precursors would be cheaper and more environmentally friendly.

#### CRedit authorship contribution statement

**Pamela Ramirez-Vidal:** Investigation, Writing – original draft, Conceptualization. **Fabián Suárez-García:** Conceptualization, Supervision, Funding acquisition, Writing – review & editing. **Rafael L.S. Canevesi:** Investigation, Formal analysis. **Alberto Castro-Muñiz:** Investigation, Formal analysis. **Philippe Gadonneix:** Investigation. **Juan Ignacio Paredes:** Conceptualization, Supervision, Funding acquisition, Writing – review & editing. **Alain Celzard:** Supervision, Writing – review & editing. **Vanessa Fierro:**

Conceptualization, Supervision, Funding acquisition, Writing - review & editing.

### Declaration of Competing Interest

The authors declare that they have no known competing financial interests or personal relationships that could have appeared to influence the work reported in this paper.

### Acknowledgements

The French research team thanks CONACYT-SENER for the scholarship 708651/ 739301 of PRV. This study was also partly supported by ANR-15-IDEX-04-LUE and TALISMAN project (2019-000214), funded by European Regional Development Fund (ERDF). Partial funding by the Spanish Ministerio de Ciencia, Innovación y Universidades, the Spanish Agencia Estatal de Investigación (AEI) and the ERDF through project RTI2018-100832-B-I00 is also gratefully acknowledged. We also thank Christine Gendarme for her technical assistance with the SEM characterisation.

### Appendix A. Supplementary material

Supplementary data to this article can be found online at <https://doi.org/10.1016/j.jcis.2021.07.104>.

### References

- [1] A. Züttel, Hydrogen Storage Methods, *Naturwissenschaften* 91 (4) (2004) 157–172, <https://doi.org/10.1007/s00114-004-0516-x>.
- [2] G.D. Berry, S.M. Aceves, Onboard Storage Alternatives for Hydrogen Vehicles, *Energy Fuels* 12 (1) (1998) 49–55, <https://doi.org/10.1021/ef9700947>.
- [3] A. Bauer, T. Mayer, M. Semmel, M.A. Guerrero Morales, J. Wind, Energetic Evaluation of Hydrogen Refueling Stations with Liquid or Gaseous Stored Hydrogen, *Int. J. Hydrog. Energy* 44 (13) (2019) 6795–6812, <https://doi.org/10.1016/j.ijhydene.2019.01.087>.
- [4] J. Zheng, L. Chen, X. Xu, L. Guo, Y. Zhou, J. Wang, A Novel Insulation System Based on Active Cooling without Power Input for Liquid Hydrogen Storage, *Energy* 182 (2019) 1–10, <https://doi.org/10.1016/j.energy.2019.06.050>.
- [5] J. Moreno-Blanco, G. Petittas, F. Espinosa-Loza, F. Elizalde-Blancas, J. Martinez-Frias, S.M. Aceves, The Storage Performance of Automotive Cryo-Compressed Hydrogen Vessels, *Int. J. Hydrog. Energy* 44 (31) (2019) 16841–16851, <https://doi.org/10.1016/j.ijhydene.2019.04.189>.
- [6] G. Sdanghi, G. Maranzana, A. Celzard, V. Fierro, Towards Non-Mechanical Hybrid Hydrogen Compression for Decentralized Hydrogen Facilities, *Energies* 13 (12) (2020) 3145, <https://doi.org/10.3390/en13123145>.
- [7] J. Bellosta von Colbe, J.-R. Ares, J. Barale, M. Baricco, C. Buckley, G. Capurso, N. Gallandat, D.M. Grant, M.N. Guzik, I. Jacob, E.H. Jensen, T. Jensen, J. Jepsen, T. Klassen, M.V. Lototskiy, K. Manickam, A. Montone, J. Puzskiel, S. Sartori, D.A. Sheppard, A. Stuart, G. Walker, C.J. Webb, H. Yang, V. Yartys, A. Züttel, M. Dornheim, Application of Hydrides in Hydrogen Storage and Compression: Achievements, Outlook and Perspectives, *Int. J. Hydrog. Energy* 44 (15) (2019) 7780–7808, <https://doi.org/10.1016/j.ijhydene.2019.01.104>.
- [8] E.M. Dematteis, N. Berti, F. Cuevas, M. Lacroche, M. Baricco, Substitutional Effects in TiFe for Hydrogen Storage: A Comprehensive Review, *Mater. Adv.* 2 (8) (2021) 2524–2560, <https://doi.org/10.1039/D1MA00101A>.
- [9] M.P. Suh, H.J. Park, T.K. Prasad, D.-W. Lim, Hydrogen Storage in Metal-Organic Frameworks, *Chem. Rev.* 112 (2) (2012) 782–835, <https://doi.org/10.1021/cr200274s>.
- [10] R. Balderas-Xicohtencatl, M. Schlichtenmayer, M. Hirscher, Volumetric Hydrogen Storage Capacity in Metal-Organic Frameworks, *Energy Technol.* 6 (3) (2018) 578–582, <https://doi.org/10.1002/ente.201700636>.
- [11] J. Juan-Juan, J.P. Marco-Lozar, F. Suárez-García, D. Cazorla-Amorós, A. Linares-Solano, A Comparison of Hydrogen Storage in Activated Carbons and a Metal-Organic Framework (MOF-5), *Carbon* 48 (10) (2010) 2906–2909, <https://doi.org/10.1016/j.carbon.2010.04.025>.
- [12] G. Sdanghi, G. Maranzana, A. Celzard, V. Fierro, Hydrogen Adsorption on Nanotextured Carbon Materials. In *Hydrogen Storage Technologies*, John Wiley & Sons Ltd (2018) 263–320, <https://doi.org/10.1002/9781119460572.ch9>.
- [13] V. Fierro, A. Szczurek, C. Zlotea, J.F. Maréché, M.T. Izquierdo, A. Albinia, M. Lacroche, G. Furdin, A. Celzard, Experimental Evidence of an Upper Limit for Hydrogen Storage at 77K on Activated Carbons, *Carbon* 48 (7) (2010) 1902–1911, <https://doi.org/10.1016/j.carbon.2010.01.052>.
- [14] M. Rzepka, P. Lamp, M.A. de la Casa-Lillo, Physisorption of Hydrogen on Microporous Carbon and Carbon Nanotubes, *J. Phys. Chem. B* 102 (52) (1998) 10894–10898, <https://doi.org/10.1021/jp9829602>.
- [15] C. Zhang, R. Kong, X. Wang, Y. Xu, F. Wang, W. Ren, Y. Wang, F. Su, J.-X. Jiang, Porous Carbons Derived from Hypercrosslinked Porous Polymers for Gas Adsorption and Energy Storage, *Carbon* 114 (2017) 608–618, <https://doi.org/10.1016/j.carbon.2016.12.064>.
- [16] Covalent Organic Frameworks and Cage Compounds: Design and Applications of Polymeric and Discrete Organic Scaffolds - Beuerle - 2018 - *Angewandte Chemie International Edition* - Wiley Online Library <https://onlinelibrary-wiley-com.bases-doc.univ-lorraine.fr/doi/abs/10.1002/anie.201710190> (accessed 2019-09-04).
- [17] J. Huang, S.R. Turner, Hypercrosslinked Polymers: A Review, *Polym. Rev.* 58 (1) (2018) 1–41, <https://doi.org/10.1080/15583724.2017.1344703>.
- [18] B. Li, R. Gong, W. Wang, X. Huang, W. Zhang, H. Li, C. Hu, B. Tan, A New Strategy to Microporous Polymers: Knitting Rigid Aromatic Building Blocks by External Cross-Linker, *Macromolecules* 44 (8) (2011) 2410–2414, <https://doi.org/10.1021/ja200630s>.
- [19] L. Tan, B. Li, X. Yang, W. Wang, B. Tan, Knitting Hypercrosslinked Conjugated Microporous Polymers with External Crosslinker, *Polymer* 70 (2015) 336–342, <https://doi.org/10.1016/j.polymer.2015.06.026>.
- [20] J. Germain, J.M.J. Fréchet, F. Svec, Nanoporous Polymers for Hydrogen Storage, *Small* 5 (10) (2009) 1098–1111, <https://doi.org/10.1002/smll.200801762>.
- [21] G. Liu, Y. Wang, C. Shen, Z. Ju, D. Yuan, A Facile Synthesis of Microporous Organic Polymers for Efficient Gas Storage and Separation, *J. Mater. Chem. A* 3 (6) (2015) 3051–3058, <https://doi.org/10.1039/C4TA05349D>.
- [22] R. Dawson, L.A. Stevens, T.C. Drage, C.E. Snape, M.W. Smith, D.J. Adams, A.I. Cooper, Impact of Water Coadsorption for Carbon Dioxide Capture in Microporous Polymer Sorbents, *J. Am. Chem. Soc.* 134 (26) (2012) 10741–10744, <https://doi.org/10.1021/ja301926h>.
- [23] R. Castaldo, G. Gentile, M. Avella, C. Carfagna, V. Ambrogio, Microporous Hyper-Crosslinked Polystyrenes and Nanocomposites with High Adsorption Properties: A Review, *Polymers* 9 (12) (2017) 651, <https://doi.org/10.3390/polym9120651>.
- [24] K. Cousins, R. Zhang, Highly Porous Organic Polymers for Hydrogen Fuel Storage, *Polymers* 11 (4) (2019) 690, <https://doi.org/10.3390/polym11040690>.
- [25] H. Ramezani-pour Penchah, A. Ghaemi, H. Ganadzadeh Gilani, Benzene-Based Hyper-Cross-Linked Polymer with Enhanced Adsorption Capacity for CO<sub>2</sub> Capture, *Energy Fuels* 33 (12) (2019) 12578–12586, <https://doi.org/10.1021/acs.energyfuels.9b03136>.
- [26] M. Saleh, H.M. Lee, K.C. Kemp, K.S. Kim, Highly Stable CO<sub>2</sub>/N<sub>2</sub> and CO<sub>2</sub>/CH<sub>4</sub> Selectivity in Hyper-Cross-Linked Heterocyclic Porous Polymers, *ACS Appl. Mater. Interfaces* 6 (10) (2014) 7325–7333, <https://doi.org/10.1021/am500728q>.
- [27] R. Vinodh, P. Hemalatha, M. Ganesh, M.M. Peng, A. Abidov, M. Palanichamy, W.S. Cha, H.-T. Jang, Novel Microporous Hypercross-Linked Conjugated Quinonoid Chromophores with Broad Light Absorption and CO<sub>2</sub> Sorption Characteristics, *RSC Adv.* 4 (8) (2014) 3678–3684, <https://doi.org/10.1039/C3RA45466E>.
- [28] H. Ramezani-pour Penchah, H. Ghanadzadeh Gilani, A. Ghaemi, CO<sub>2</sub>, N<sub>2</sub>, and H<sub>2</sub> Adsorption by Hyper-Cross-Linked Polymers and Their Selectivity Evaluation by Gas-Solid Equilibrium, *J. Chem. Eng. Data* (2020), <https://doi.org/10.1021/acs.jced.0c00541>.
- [29] H. Gao, L. Ding, H. Bai, A. Liu, S. Li, L. Li, Pitch-Based Hyper-Cross-Linked Polymers with High Performance for Gas Adsorption, *J. Mater. Chem. A* 4 (42) (2016) 16490–16498, <https://doi.org/10.1039/C6TA07033G>.
- [30] J. Germain, J. Hradil, J.M.J. Fréchet, F. Svec, High Surface Area Nanoporous Polymers for Reversible Hydrogen Storage, *Chem. Mater.* 18 (18) (2006) 4430–4435, <https://doi.org/10.1021/cm061186p>.
- [31] J. Germain, J.M.J. Fréchet, F. Svec, Hypercrosslinked Polyanilines with Nanoporous Structure and High Surface Area: Potential Adsorbents for Hydrogen Storage, *J. Mater. Chem.* 17 (47) (2007) 4989–4997, <https://doi.org/10.1039/B711509A>.
- [32] B. Li, R. Gong, Y. Luo, B. Tan, Tailoring the Pore Size of Hypercrosslinked Polymers, *Soft Matter* 7 (22) (2011) 10910–10916, <https://doi.org/10.1039/C1SM06113E>.
- [33] X. Yang, M. Yu, Y. Zhao, C. Zhang, X. Wang, J.-X. Jiang, Hypercrosslinked Microporous Polymers Based on Carbazole for Gas Storage and Separation, *RSC Adv.* 4 (105) (2014) 61051–61055, <https://doi.org/10.1039/C4RA09394A>.
- [34] B. Li, X. Huang, L. Liang, B. Tan, Synthesis of Uniform Microporous Polymer Nanoparticles and Their Applications for Hydrogen Storage, *J. Mater. Chem.* 20 (35) (2010) 7444–7450, <https://doi.org/10.1039/C0JM01423K>.
- [35] C. Gu, Y. Bao, W. Huang, D. Liu, R. Yang, Four Simple Structure Carbazole-Based Conjugated Microporous Polymers with Different Soft Connected Chains, *Macromol. Chem. Phys.* 217 (6) (2016) 748–756, <https://doi.org/10.1002/macp.201500420>.
- [36] Y. Luo, S. Zhang, Y. Ma, W. Wang, B. Tan, Microporous Organic Polymers Synthesized by Self-Condensation of Aromatic Hydroxymethyl Monomers, *Polym. Chem.* 4 (4) (2013) 1126–1131, <https://doi.org/10.1039/C2PY20914D>.
- [37] S. Wang, L. Tan, C. Zhang, I. Hussain, B. Tan, Novel POSS-Based Organic-Inorganic Hybrid Porous Materials by Low Cost Strategies, *J. Mater. Chem. A* 3 (12) (2015) 6542–6548, <https://doi.org/10.1039/C4TA06963C>.
- [38] Y. Luo, B. Li, W. Wang, K. Wu, B. Tan, Hypercrosslinked Aromatic Heterocyclic Microporous Polymers: A New Class of Highly Selective CO<sub>2</sub> Capturing Materials, *Adv. Mater.* 24 (42) (2012) 5703–5707, <https://doi.org/10.1002/adma.201202447>.
- [39] R. Dawson, T. Ratvijitvech, M. Corker, A. Laybourn, Y.Z. Khimyak, A.I. Cooper, D.J. Adams, Microporous Copolymers for Increased Gas Selectivity, *Polym. Chem.* 3 (8) (2012) 2034–2038, <https://doi.org/10.1039/C2PY20136D>.

- [40] J.-Y. Lee, C.D. Wood, D. Bradshaw, M.J. Rosseinsky, A.I. Cooper, Hydrogen Adsorption in Microporous Hypercrosslinked Polymers, *Chem. Commun.* 25 (2006) 2670–2672, <https://doi.org/10.1039/B604625H>.
- [41] G. Gatti, M. Errahali, L. Tei, M. Cossi, L. Marchese, On the Gas Storage Properties of 3D Porous Carbons Derived from Hyper-Crosslinked Polymers, *Polymers* 11 (4) (2019) 588, <https://doi.org/10.3390/polym11040588>.
- [42] C.D. Wood, B. Tan, A. Trewin, H. Niu, D. Bradshaw, M.J. Rosseinsky, Y.Z. Khimyak, N.L. Campbell, R. Kirk, E. Stöckel, A.I. Cooper, Hydrogen Storage in Microporous Hypercrosslinked Organic Polymer Networks, *Chem. Mater.* 19 (8) (2007) 2034–2048, <https://doi.org/10.1021/cm070356a>.
- [43] N.F. Attia, M. Jung, J. Park, S.-Y. Cho, H. Oh, Facile Synthesis of Hybrid Porous Composites and Its Porous Carbon for Enhanced H<sub>2</sub> and CH<sub>4</sub> Storage, *Int. J. Hydrog. Energy* 45 (57) (2020) 32797–32807, <https://doi.org/10.1016/j.ijhydene.2020.03.004>.
- [44] L. Nikoshvili, E. Shimanskaya, A. Bykov, I. Yuranov, L. Kiwi-Minsker, E. Sulman, Selective Hydrogenation of 2-Methyl-3-Butyn-2-Ol over Pd-Nanoparticles Stabilized in Hypercrosslinked Polystyrene: Solvent Effect, *Catal. Today* 241 (2015) 179–188, <https://doi.org/10.1016/j.cattod.2014.01.045>.
- [45] R. Castaldo, R. Avolio, M. Cocca, G. Gentile, M.E. Errico, M. Avella, C. Carfagna, V. Ambrogio, Synthesis and Adsorption Study of Hyper-Crosslinked Styrene-Based Nanocomposites Containing Multi-Walled Carbon Nanotubes, *RSC Adv.* 7 (12) (2017) 6865–6874, <https://doi.org/10.1039/C6RA25481K>.
- [46] R. Castaldo, R. Avolio, M. Cocca, G. Gentile, M.E. Errico, M. Avella, C. Carfagna, V. Ambrogio, A Versatile Synthetic Approach toward Hyper-Cross-Linked Styrene-Based Polymers and Nanocomposites, *Macromolecules* 50 (11) (2017) 4132–4143, <https://doi.org/10.1021/acs.macromol.7b00812>.
- [47] A.T. Smith, A.M. LaChance, S. Zeng, B. Liu, L. Sun, Synthesis, Properties, and Applications of Graphene Oxide/Reduced Graphene Oxide and Their Nanocomposites, *Nano Mater. Sci.* 1 (1) (2019) 31–47, <https://doi.org/10.1016/j.nanoms.2019.02.004>.
- [48] W.S. Hummers, R.E. Offeman, Preparation of Graphitic Oxide, *J. Am. Chem. Soc.* 80 (6) (1958) 1339, <https://doi.org/10.1021/ja01539a017>.
- [49] J.I. Paredes, S. Villar-Rodil, A. Martínez-Alonso, J.M.D. Tascón, Graphene Oxide Dispersions in Organic Solvents, *Langmuir* 24 (19) (2008) 10560–10564, <https://doi.org/10.1021/la801744a>.
- [50] J. Rouquerol, P. Llewellyn, F. Rouquerol, Is the BET Equation Applicable to Microporous Adsorbents? in: P.L. Llewellyn, F. Rodríguez-Reinoso, J. Rouquerol, N. Seaton (Eds.) *Studies in Surface Science and Catalysis; Characterization of Porous Solids VII*; Elsevier, 2007; vol. 160, pp 49–56. [10.1016/S0167-2991\(07\)80008-5](https://doi.org/10.1016/S0167-2991(07)80008-5).
- [51] J. Jagiello, J. Kevin, A. Celzard, V. Fierro, Enhanced Resolution of Ultra Micropore Size Determination of Biochars and Activated Carbons by Dual Gas Analysis Using N<sub>2</sub> and CO<sub>2</sub> with 2D-NLDFT Adsorption Models, *Carbon* 144 (2019) 206–215, <https://doi.org/10.1016/j.carbon.2018.12.028>.
- [52] J. Jagiello, C. Ania, J.B. Parra, C. Cook, Dual Gas Analysis of Microporous Carbons Using 2D-NLDFT Heterogeneous Surface Model and Combined Adsorption Data of N<sub>2</sub> and CO<sub>2</sub>, *Carbon* 91 (2015) 330–337, <https://doi.org/10.1016/j.carbon.2015.05.004>.
- [53] J. Jagiello, J. Kevin, C.O. Ania, J.B. Parra, A. Celzard, V. Fierro, Exploiting the Adsorption of Simple Gases O<sub>2</sub> and H<sub>2</sub> with Minimal Quadrupole Moments for the Dual Gas Characterization of Nanoporous Carbons Using 2D-NLDFT Models, *Carbon* 160 (2020) 164–175, <https://doi.org/10.1016/j.carbon.2020.01.013>.
- [54] Y. Wang, Q. He, H. Qu, X. Zhang, J. Guo, J. Zhu, G. Zhao, H.A. Colorado, J. Yu, L. Sun, S. Bhana, M.A. Khan, X. Huang, D.P. Young, H. Wang, X. Wang, S. Wei, Z. Guo, Magnetic Graphene Oxide Nanocomposites: Nanoparticles Growth Mechanism and Property Analysis, *J. Mater. Chem. C* 2 (44) (2014) 9478–9488, <https://doi.org/10.1039/C4TC01351D>.
- [55] S. Vyazovkin, Thermogravimetric Analysis. In *Characterization of Materials*, Am. Cancer Soc. (2012) 1–12, <https://doi.org/10.1002/0471266965.com029.pub2>.
- [56] M. Errahali, G. Gatti, L. Tei, G. Paul, G.A. Rolla, L. Canti, A. Fraccarollo, M. Cossi, A. Comotti, P. Sozzani, L. Marchese, Microporous Hyper-Cross-Linked Aromatic Polymers Designed for Methane and Carbon Dioxide Adsorption, *J. Phys. Chem. C* 118 (49) (2014) 28699–28710, <https://doi.org/10.1021/jp5096695>.
- [57] D. Fang, X. Li, M. Zou, X. Guo, A. Zhang, Carbazole-Functionalized Hyper-Cross-Linked Polymers for CO<sub>2</sub> Uptake Based on Friedel-Crafts Polymerization on 9-Phenylcarbazole, *Beilstein J. Org. Chem.* 15 (2019) 2856–2863, <https://doi.org/10.3762/bjoc.15.279>.
- [58] M. Rodríguez-Baeza, C.A. Neira, J.C. Aguilera, Thermogravimetric Study of the Formation of Cross-Linked Structures in the Synthesis of Poly (Methylsiloxane), *J. Chil. Chem. Soc.* 48 (2) (2003) 75–77, <https://doi.org/10.4067/S0717-97072003000200013>.
- [59] V. Davankov, M.P. Tsyurupa, *Hypercrosslinked Polymeric Networks and Adsorbing Materials: Synthesis, Properties, Structure, and Applications, 1st edition.*, Elsevier, Amsterdam Heidelberg, 2010.
- [60] S. Hou, S. Razzaque, B. Tan, Effects of Synthesis Methodology on Microporous Organic Hyper-Cross-Linked Polymers with Respect to Structural Porosity, Gas Uptake Performance and Fluorescence Properties, *Polym. Chem.* 10 (11) (2019) 1299–1311, <https://doi.org/10.1039/C8PY01730A>.
- [61] C. Wilson, M.J. Main, N.J. Cooper, M.E. Briggs, A.I. Cooper, D.J. Adams, Swellable Functional Hypercrosslinked Polymer Networks for the Uptake of Chemical Warfare Agents, *Polym. Chem.* 8 (12) (2017) 1914–1922, <https://doi.org/10.1039/C7PY00040E>.
- [62] S. Villar-Rodil, J.I. Paredes, A. Martínez-Alonso, J.M.D. Tascón, Atomic Force Microscopy and Infrared Spectroscopy Studies of the Thermal Degradation of Nomex Aramid Fibers, *Chem. Mater.* 13 (11) (2001) 4297–4304, <https://doi.org/10.1021/cm001219f>.
- [63] F. Suárez-García, A. Martínez-Alonso, J.M.D. Tascón, Pyrolysis of Apple Pulp: Effect of Operation Conditions and Chemical Additives, *J. Anal. Appl. Pyrolysis* 62 (1) (2002) 93–109, [https://doi.org/10.1016/S0165-2370\(00\)00216-3](https://doi.org/10.1016/S0165-2370(00)00216-3).
- [64] F. Suárez-García, A. Martínez-Alonso, J.M.D. Tascón, A Comparative Study of the Thermal Decomposition of Apple Pulp in the Absence and Presence of Phosphoric Acid, *Polym. Degrad. Stab.* 75 (2) (2002) 375–383, [https://doi.org/10.1016/S0141-3910\(01\)00243-9](https://doi.org/10.1016/S0141-3910(01)00243-9).
- [65] Carey, F. A.; Sundberg, R. J. *Aromatic Substitution*, in: F.A. Carey, R.J. Sundberg (Eds.), *Advanced Organic Chemistry: Part A: Structure and Mechanisms, Advanced Organic Chemistry*; Springer US: Boston, MA, 2007; pp. 771–831. [10.1007/978-0-387-44899-2\\_9](https://doi.org/10.1007/978-0-387-44899-2_9).
- [66] J.I. Paredes, S. Villar-Rodil, P. Solís-Fernández, A. Martínez-Alonso, J.M.D. Tascón, Atomic Force and Scanning Tunneling Microscopy Imaging of Graphene Nanosheets Derived from Graphite Oxide, *Langmuir* 25 (10) (2009) 5957–5968, <https://doi.org/10.1021/la804216z>.
- [67] S. Stankovich, D.A. Dikin, R.D. Piner, K.A. Kohlhaas, A. Kleinhammes, Y. Jia, Y. Wu, S.T. Nguyen, R.S. Ruoff, Synthesis of Graphene-Based Nanosheets via Chemical Reduction of Exfoliated Graphite Oxide, *Carbon* 45 (7) (2007) 1558–1565, <https://doi.org/10.1016/j.carbon.2007.02.034>.
- [68] F. Björnerbäck, N. Hedin, Highly Porous Hypercrosslinked Polymers Derived from Biobased Molecules, *ChemSusChem* 12 (4) (2019) 839–847, <https://doi.org/10.1002/cssc.201802681>.
- [69] Z. Wu, R.P. Rodgers, A.G. Marshall, Two- and Three-Dimensional van Krevelen Diagrams: A Graphical Analysis Complementary to the Kendrick Mass Plot for Sorting Elemental Compositions of Complex Organic Mixtures Based on Ultrahigh-Resolution Broadband Fourier Transform Ion Cyclotron Resonance Mass Measurements, *Anal. Chem.* 76 (9) (2004) 2511–2516, <https://doi.org/10.1021/ac0355449>.
- [70] F.S. Macintyre, D.C. Sherrington, L. Tetley, Synthesis of Ultrahigh Surface Area Monodisperse Porous Polymer Nanospheres, *Macromolecules* 39 (16) (2006) 5381–5384, <https://doi.org/10.1021/ma0610010>.
- [71] J. Jeromenok, J. Weber, Restricted Access: On the Nature of Adsorption/Desorption Hysteresis in Amorphous, Microporous Polymeric Materials, *Langmuir* 29 (42) (2013) 12982–12989, <https://doi.org/10.1021/la402630s>.
- [72] B. Lopez-Iglesias, F. Suárez-García, C. Aguilar-Lugo, A. González Ortega, C. Bartolomé, J.M. Martínez-Illarduya, J.G. de la Campa, Á.E. Lozano, C. Álvarez, Microporous Polymer Networks for Carbon Capture Applications, *ACS Appl. Mater. Interfaces* 10 (31) (2018) 26195–26205, <https://doi.org/10.1021/acsmi.8b05854>.
- [73] B.S. Ghanem, M. Hashem, K.D.M. Harris, K.J. Msayib, M. Xu, P.M. Budd, N. Chaukura, D. Book, S. Tedds, A. Walton, N.B. McKeown, Triptycene-Based Polymers of Intrinsic Microporosity: Organic Materials That Can Be Tailored for Gas Adsorption, *Macromolecules* 43 (12) (2010) 5287–5294, <https://doi.org/10.1021/ma100640m>.
- [74] M. Heuchel, D. Fritsch, P.M. Budd, N.B. McKeown, D. Hofmann, Atomistic Packing Model and Free Volume Distribution of a Polymer with Intrinsic Microporosity (PIM-1), *J. Membr. Sci.* 318 (1) (2008) 84–99, <https://doi.org/10.1016/j.memsci.2008.02.038>.
- [75] J. Weber, M. Antonietti, A. Thomas, Microporous Networks of High-Performance Polymers: Elastic Deformations and Gas Sorption Properties, *Macromolecules* 41 (8) (2008) 2880–2885, <https://doi.org/10.1021/ma702495r>.
- [76] M. Thommes, K. Kaneko, A.V. Neimark, J.P. Olivier, F. Rodríguez-Reinoso, J. Rouquerol, K.S.W. Sing, Physisorption of Gases, with Special Reference to the Evaluation of Surface Area and Pore Size Distribution (IUPAC Technical Report), *Pure Appl. Chem.* 87 (9–10) (2015) 1051–1069, <https://doi.org/10.1515/pac-2014-1117>.
- [77] J.-S.M. Lee, M.E. Briggs, T. Hasell, A.I. Cooper, Hyperporous Carbons from Hypercrosslinked Polymers, *Adv. Mater.* 28 (44) (2016) 9804–9810, <https://doi.org/10.1002/adma.201603051>.
- [78] L. Pan, Q. Chen, J.-H. Zhu, J.-G. Yu, Y.-J. He, B.-H. Han, Hypercrosslinked Porous Polycarbazoles via One-Step Oxidative Coupling Reaction and Friedel-Crafts Alkylation, *Polym. Chem.* 6 (13) (2015) 2478–2487, <https://doi.org/10.1039/C4PY01797H>.
- [79] J. Jagiello, W. Betz, Characterization of Pore Structure of Carbon Molecular Sieves Using DFT Analysis of Ar and H<sub>2</sub> Adsorption Data, *Microporous Mesoporous Mater.* 108 (1) (2008) 117–122, <https://doi.org/10.1016/j.micromeso.2007.03.035>.
- [80] J. Jagiello, C.O. Ania, J.B. Parra, L. Jagiello, J.J. Pis, Using DFT Analysis of Adsorption Data of Multiple Gases Including H<sub>2</sub> for the Comprehensive Characterization of Microporous Carbons, *Carbon* 45 (5) (2007) 1066–1071, <https://doi.org/10.1016/j.carbon.2006.12.011>.
- [81] A. Peigney, Ch. Laurent, E. Flahaut, R.R. Bacsa, A. Rousset, Specific Surface Area of Carbon Nanotubes and Bundles of Carbon Nanotubes, *Carbon* 39 (4) (2001) 507–514, [https://doi.org/10.1016/S0008-6223\(00\)00155-X](https://doi.org/10.1016/S0008-6223(00)00155-X).
- [82] M.F. de Lange, L.-C. Lin, J. Gascon, T.J.H. Vlucht, F. Kapteijn, Assessing the Surface Area of Porous Solids: Limitations, Probe Molecules, and Methods, *Langmuir* 32 (48) (2016) 12664–12675, <https://doi.org/10.1021/acs.langmuir.6b03531>.
- [83] J. Jagiello, M. Thommes, Comparison of DFT Characterization Methods Based on N<sub>2</sub>, Ar, CO<sub>2</sub>, and H<sub>2</sub> Adsorption Applied to Carbons with Various Pore Size

- Distributions, *Carbon* 42 (7) (2004) 1227–1232, <https://doi.org/10.1016/j.carbon.2004.01.022>.
- [84] X. Yu, Z. Tang, D. Sun, L. Ouyang, M. Zhu, Recent Advances and Remaining Challenges of Nanostructured Materials for Hydrogen Storage Applications, *Prog. Mater. Sci.* 88 (2017) 1–48, <https://doi.org/10.1016/j.pmatsci.2017.03.001>.
- [85] E. García-Díez, S. Schaefer, A. Sanchez-Sanchez, A. Celzard, V. Fierro, M.M. Maroto-Valer, S. García, Novel Porous Carbons Derived from Coal Tar Rejects: Assessment of the Role of Pore Texture in CO<sub>2</sub> Capture under Realistic Postcombustion Operating Temperatures, *ACS Appl. Mater. Interfaces* 11 (40) (2019) 36789–36799, <https://doi.org/10.1021/acsami.9b13247>.
- [86] T. Islamoglu, S. Behera, Z. Kahveci, T.-D. Tessema, P. Jena, H.M. El-Kaderi, Enhanced Carbon Dioxide Capture from Landfill Gas Using Bifunctionalized Benzimidazole-Linked Polymers, *ACS Appl. Mater. Interfaces* 8 (23) (2016) 14648–14655, <https://doi.org/10.1021/acsami.6b05326>.
- [87] Z. Bacsik, N. Ahlsten, A. Ziadi, G. Zhao, A.E. Garcia-Bennett, B. Martín-Matute, N. Hedin, Mechanisms and Kinetics for Sorption of CO<sub>2</sub> on Bicontinuous Mesoporous Silica Modified with *n*-Propylamine, *Langmuir* 27 (17) (2011) 11118–11128, <https://doi.org/10.1021/la202033p>.
- [88] K.E. Hurst, T. Gennett, J. Adams, M.D. Allendorf, R. Balderas-Xicohtencatl, M. Bielewski, B. Edwards, L. Espinal, B. Fultz, M. Hirscher, M.S.L. Hudson, Z. Hulvey, M. Latroche, D.-J. Liu, M. Kapelewski, E. Napolitano, Z.T. Perry, J. Purewal, V. Stavila, M. Veenstra, J.L. White, Y. Yuan, H.-C. Zhou, C. Zlotea, P. Parilla, An International Laboratory Comparison Study of Volumetric and Gravimetric Hydrogen Adsorption Measurements, *ChemPhysChem* 20 (15) (2019) 1997–2009, <https://doi.org/10.1002/cphc.201900166>.
- [89] S. Yuan, D. White, A. Mason, D.-J. Liu, Porous Organic Polymers Containing Carborane for Hydrogen Storage, *Int. J. Energy Res.* 37 (7) (2013) 732–740, <https://doi.org/10.1002/er.1886>.
- [90] J. Wang, W. Sng, G. Yi, Y. Zhang, Imidazolium Salt-Modified Porous Hypercrosslinked Polymers for Synergistic CO<sub>2</sub> Capture and Conversion, *Chem. Commun.* 51 (60) (2015) 12076–12079, <https://doi.org/10.1039/C5CC04702A>.
- [91] M.G. Schwab, A. Lennert, J. Pahnke, G. Jonschker, M. Koch, I. Senkovska, M. Rehahn, S. Kaskel, Nanoporous Copolymer Networks through Multiple Friedel–Crafts-Alkylation—Studies on Hydrogen and Methane Storage, *J. Mater. Chem.* 21 (7) (2011) 2131–2135, <https://doi.org/10.1039/C0JM03017A>.
- [92] J. Germain, F. Svec, J.M.J. Fréchet, Preparation of Size-Selective Nanoporous Polymer Networks of Aromatic Rings: Potential Adsorbents for Hydrogen Storage, *Chem. Mater.* 20 (22) (2008) 7069–7076, <https://doi.org/10.1021/cm802157r>.
- [93] P. Ramirez-Vidal, R.L.S. Canevesi, G. Sdanghi, S. Schaefer, G. Maranzana, A. Celzard, V. Fierro, A Step Forward in Understanding the Hydrogen Adsorption and Compression on Activated Carbons, *ACS Appl. Mater. Interfaces* 13 (10) (2021) 12562–12574, <https://doi.org/10.1021/acsami.0c22192>.
- [94] G. Sdanghi, V. Nicolas, K. Mozet, S. Schaefer, G. Maranzana, A. Celzard, V. Fierro, A 70 MPa Hydrogen Thermally Driven Compressor Based on Cyclic Adsorption-Desorption on Activated Carbon, *Carbon* 161 (2020) 466–478, <https://doi.org/10.1016/j.carbon.2020.01.099>.
- [95] N.B. McKeown, B. Gahnem, K.J. Msayib, P.M. Budd, C.E. Tattershall, K. Mahmood, S. Tan, D. Book, H.W. Langmi, A. Walton, Towards Polymer-Based Hydrogen Storage Materials: Engineering Ultramicroporous Cavities within Polymers of Intrinsic Microporosity, *Angew. Chem. Int. Ed.* 45 (11) (2006) 1804–1807, <https://doi.org/10.1002/anie.200504241>.
- [96] J. Park, M. Jung, H. Jang, K. Lee, N.F. Attia, H. Oh, A Facile Synthesis Tool of Nanoporous Carbon for Promising H<sub>2</sub>, CO<sub>2</sub>, and CH<sub>4</sub> Sorption Capacity and Selective Gas Separation, *J. Mater. Chem. A* 6 (45) (2018) 23087–23100, <https://doi.org/10.1039/C8TA08603F>.
- [97] E. Poirier, R. Chahine, T.K. Bose, Hydrogen Adsorption in Carbon Nanostructures, *Int. J. Hydrog. Energy* 26 (8) (2001) 831–835, [https://doi.org/10.1016/S0360-3199\(01\)00014-3](https://doi.org/10.1016/S0360-3199(01)00014-3).
- [98] M.C. Tellez-Juárez, V. Fierro, W. Zhao, N. Fernández-Huerta, M.T. Izquierdo, E. Reguera, A. Celzard, Hydrogen Storage in Activated Carbons Produced from Coals of Different Ranks: Effect of Oxygen Content, *Int. J. Hydrog. Energy* 39 (10) (2014) 4996–5002, <https://doi.org/10.1016/j.ijhydene.2014.01.071>.
- [99] Z. Weigang, V. Fierro, C. Zlotea, E. Aylon, M.T. Izquierdo, M. Latroche, A. Celzard, Optimization of Activated Carbons for Hydrogen Storage, *Int. J. Hydrog. Energy* 36 (2011) 11746–11751, <https://doi.org/10.1016/j.ijhydene.2011.05.181>.
- [100] W. Zhao, V. Fierro, C. Zlotea, E. Aylon, M.T. Izquierdo, M. Latroche, A. Celzard, Activated Carbons with Appropriate Micropore Size Distribution for Hydrogen Adsorption, *Int. J. Hydrog. Energy* 36 (9) (2011) 5431–5434, <https://doi.org/10.1016/j.ijhydene.2010.12.137>.
- [101] W. Zhao, V. Fierro, N. Fernández-Huerta, M.T. Izquierdo, A. Celzard, Impact of Synthesis Conditions of KOH Activated Carbons on Their Hydrogen Storage Capacities, *Int. J. Hydrog. Energy* 37 (19) (2012) 14278–14284, <https://doi.org/10.1016/j.ijhydene.2012.06.110>.